FLOW DIVERGENCE AROUND A VERTICAL AXIS WIND TURBINE

A NUMERICAL STUDY ON THE FLOW DIVERGENCE AROUND A HIGH SOLIDITY VERTICAL AXIS WIND TURBINE

BY

GREG MISNER, B. ENG

A Thesis Submitted to the School of Graduate Studies

In Partial Fulfillment of the Requirements

For the Degree

Masters of Applied Science

McMaster University

©Copyright by Greg Misner, February 2019

MASTERS OF APPLIED SCIENCE (2019) McMaster University

(Mechanical Engineering) Hamilton, ON

Title: A numerical study on the flow divergence around a high solidity vertical axis wind turbine

Author: Greg Misner, B. Eng

Supervisor: Dr. Stephen Tullis

Number of pages: xviii, 88

Abstract

This thesis reports on a numerical investigation into the three-dimensional flow divergence around a high solidity vertical axis wind turbine. Three-dimensional unsteady Reynolds averaged Navier-Stokes simulations of an H-type vertical axis wind turbine were used to examine the impact of turbine aspect ratio and tip speed ratio on the flow divergence. The turbine height was changed to alter the turbine aspect ratio, while keeping the diameter constant, to ensure that the solidity and tip speed ratio values were comparable between the different aspect ratios tested.

The power output of the turbine consistently increased with aspect ratio and the optimal tip speed ratio for peak performance was negligibly affected. The flow divergence results showed that larger aspect ratio turbines had significantly more flow divergence with a 1 m/s entrance velocity difference between the smallest and largest cases. These two results where contradictory as a larger aspect ratio turbine was more efficient even though it had a smaller fraction of the upstream flow entering the upwind pass. The reason for this result was that impact of the tip effects, which caused a power reduction near the end of the blades. The distance from the blade tips that experienced a power reduction was constant for turbines of aspect ratio one and greater, resulting in a smaller turbine having a greater fraction of its height effected by the tips. This caused the overall power output for a smaller aspect ratio turbine to be lower even though its centre performance was higher, due to an

increased entrance velocity.

The change in flow divergence with tip speed ratio was also examined to better understand the driving force behind the divergence. It was found that the turbine power output was not the direct cause of flow divergence. The blade forces, specifically the force generated in the upstream direction had a strong linear correlation with the upstream flow divergence.

Acknowledgments

First and foremost I would like to thank my supervisor Dr. Stephen Tullis for his invaluable support, expertise, and guidance. Without his help I would not have had this interesting research opportunity or successfully completed this thesis.

Thanks also goes to my fellow graduate students in the thermo fluids lab for making our lab a great work environment. Special thanks goes to Brianna Harris for always being willing to help and give advice based on her experience as a masters and PhD student, and Cam Galipeau who started his masters at the same time and was there to help tackle common problems as we progressed.

I would like to thank my friends and family, for their support throughout this endeavor and assistance in teaching me to become a better writer. I am also thankful for the financial support from the Ontario Graduate Scholarship program for making this research opportunity possible.

Contents

List of Figures

List of Tables

Nomenclature

English Characters

c	turbine blade chord length [m]
C_f	coefficient of force, dimensionless ratio of turbine blade force to total force in the wind
C_p	coefficient of power, dimensionless ratio of turbine power output to total kinetic energy available in the wind
D	turbine diameter [m]
H	turbine height [m]
k	turbulent kinetic energy [W]
N	number of blades
P	pressure [KPa]
P_{out}	turbine power output [W]
P_k	turbulent production
r	turbine radius [m]
Re_{chord}	Reynolds number based on the airfoil chord length
S	projected or swept area of turbine [m^2]
S_{ij}	strain rate tensor
U_∞	infinitely far upstream wind velocity [m/s]
U_{rot}	velocity component due to turbine rotation [m/s]
U	blade incident wind velocity vector [m/s]

Greek Characters

α	angle of attack, angle between wind vector U and chord line [degrees]
ϵ	turbulence dissipation rate [J/kg s]
Γ	Circulation
κ	McLaren's velocity correction factor
λ	tip speed ratio, ratio of turbine blade speed to infinite wind velocity
ν	air viscosity [Kg/ms]
ν_T	turbulent eddy viscosity
ρ	air density [Kg/m^3]
σ	turbine solidity - dimensionless ratio of total turbine blade area to turbine swept area
τ	McLaren's height correction factor
θ	blade position around turbine [degrees]
ω	turbine angular velocity [rad/s]
ω	specific turbulence dissipation rate [1/s]

Abbreviations

2D	two-dimensional
3D	three-dimensional
AoA	angle of attack
AR	turbine aspect ratio (H/D)
CFD	computational fluid dynamics
HAWT	horizontal axis wind turbine
LES	large eddy simulation
RPM	revolutions per minute
TSR	tip speed ratio
URANS	unsteady Reynolds averaged Navier-Stokes
VAWT	vertical axis wind turbine

Chapter 1: Introduction

1.1 Thesis Statement

Computational fluid dynamics analysis was performed on a high solidity vertical axis wind turbine to examine the impact of turbine aspect ratio and tip speed ratio on the flow divergence around a vertical axis wind turbine.

1.2 Motivation

Climate change makes the need to find clean and renewable sources of energy production critical to ensuring a more environmentally sustainable and sufficient reliable electricity supply. Wind energy is currently one of the leading sources of renewable energy and installations come in varying sizes, from large industrial wind farms to small turbines on houses and cottages.

There are two main types of wind turbines: horizontal axis wind turbines (HAWTs) and vertical axis wind turbines (VAWTs). Both turbine designs use aerodynamic lift to produce power. Varying structural shapes exist for each, which come with their own advantages and disadvantages. HAWTs are currently the most common commercial wind turbine, and resemble a typical windmill or fan. They are considered to be more efficient then VAWTs for large scale industrial wind farms, but require a location with relatively consistent wind direction since they must rotate around to face the incoming wind.

VAWTs that use lift to produce power are called Darrieus wind turbines and typically come in two different styles; a troposkein shape VAWT or a straight bladed H-type VAWT (Figure 1). Due to their symmetrical three dimensional shape, no active yaw control is required, which gives them an advantage in locations with rapidly changing wind direction. In additional, a VAWTs generator is located at the base of the turbine, allowing for easier and cheaper maintenance. Many of the advantages attributed to VAWTs indicate that they would be more effective then HAWTs for small scale installations in locations that have highly unpredictable wind conditions.

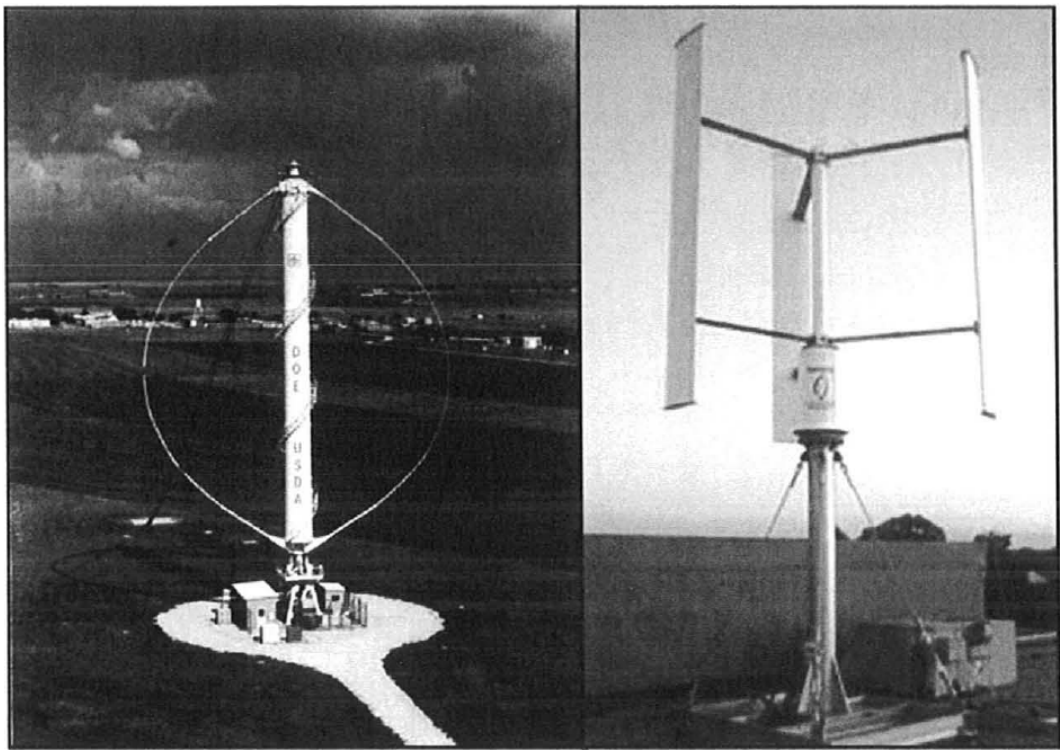

Figure 1: A troposkein shape VAWT (left) and straight bladed H-type VAWT (right). (Fiedler, 2009)

VAWTs are commonly classified by their solidity, which is the ratio of

the total blade surface area to the rotor projected area. Turbines with a high solidity have been found to operate most effectively at a low rotational velocity. When operating at a low rotation velocity, the blades of the turbine experience a large range of incoming wind angles or angle of attack (AoA), causing dynamic stall to occur over the blades. Accurately modeling such effects is difficult and much of the research to date on high solidity VAWTs has focused on the small details in the flow or simply analyzed the power output for different geometries. Very little research has focused on the large scale aerodynamics that occur around a high solidity VAWTs, especially the behaviour of the flow upstream of the turbine.

From classical analysis methods of wind turbine performance, like stream-tube analysis, it is know that the reduction in wind velocity approaching a turbine significantly affects the turbines efficiency. This reduction in approaching wind velocity represents the amount of flow diverging around the turbine upstream. Although the flow divergence around a HAWT is extremely well understood, the more complex 3D flow divergence around a VAWT has not been studied. This study aims to increase the knowledge of the overall upstream flow divergence to better understand the aerodynamics around a high solidity VAWT and its connection with turbine performance.

1.3 Objectives

This research aims to develop an understanding of the aerodynamics upstream and inside of a VAWT, as well as the effect of turbine size on these flows. The resulting power efficiency is also analyzed, to see how it might relate to the aerodynamic characteristics. Previous studies on the flow field around a VAWT have typically been experimental in nature, which limits them to a single turbine size. To more effectively study these flow fields for a wider range of turbine sizes, numerical methods were used, specifically three-dimensional (3D) computational fluid dynamics (CFD) analyze. The use of CFD for VAWT studies over the last decade has shown that they can accurately simulate the flow field and performance of a VAWT.

1.4 Thesis Layout

This thesis is comprised of five chapters: an introduction, three technical chapters that outline the research, and a conclusion. The introduction describes the motivation and objectives of the present research and outlines the layout of the thesis. Chapter 2 provides technical background information on VAWTs, and a comprehensive review of the current state of literature related to this study. Chapter 3 discusses the CFD modeling of VAWTs and the turbine geometry tested. The numerical results are presented and discussed in Chapter 4. Finally, the conclusions and scientific contributions of this study are summarized in Chapter 5.

Chapter 2: Background

This chapter begins with an explanation of the principles of VAWT operation, followed by the definition of dimensionless coefficients associated with VAWTs. The rest of the chapter explores literature on VAWTs, with an end focus on the 3D flow field, mainly studied using 3D CFD analysis.

2.1 Vertical Axis Wind Turbine Operation

To explain how a vertical axis wind turbine operates, a quasi-steady state analysis is typically used. Figure 2 shows the top view of a VAWT, labeled with important variables used to describe the turbine operation.

As the turbine rotates, the blades will experience a flow velocity that is tangential to the blades rotational path (U_{rot}). When there is no incoming wind velocity ($U_\infty = 0$ m/s), a blade will only experience the rotational velocity that always has an AoA equal to zero. During normal operation of the turbine, when there is a non-zero incoming wind velocity ($U_\infty > 0$ m/s), a blade will experience a relative wind velocity (U) that is the summation of the incoming wind velocity and rotational velocity vectors. This relative wind velocity will have a non-zero AoA, resulting in the blades experiencing a lift and drag force. These lift and drag forces can be resolved into a radial and tangential component, where the tangential force acts as a thrust force driving the production of power. The relative velocity, AoA, and resulting tangential

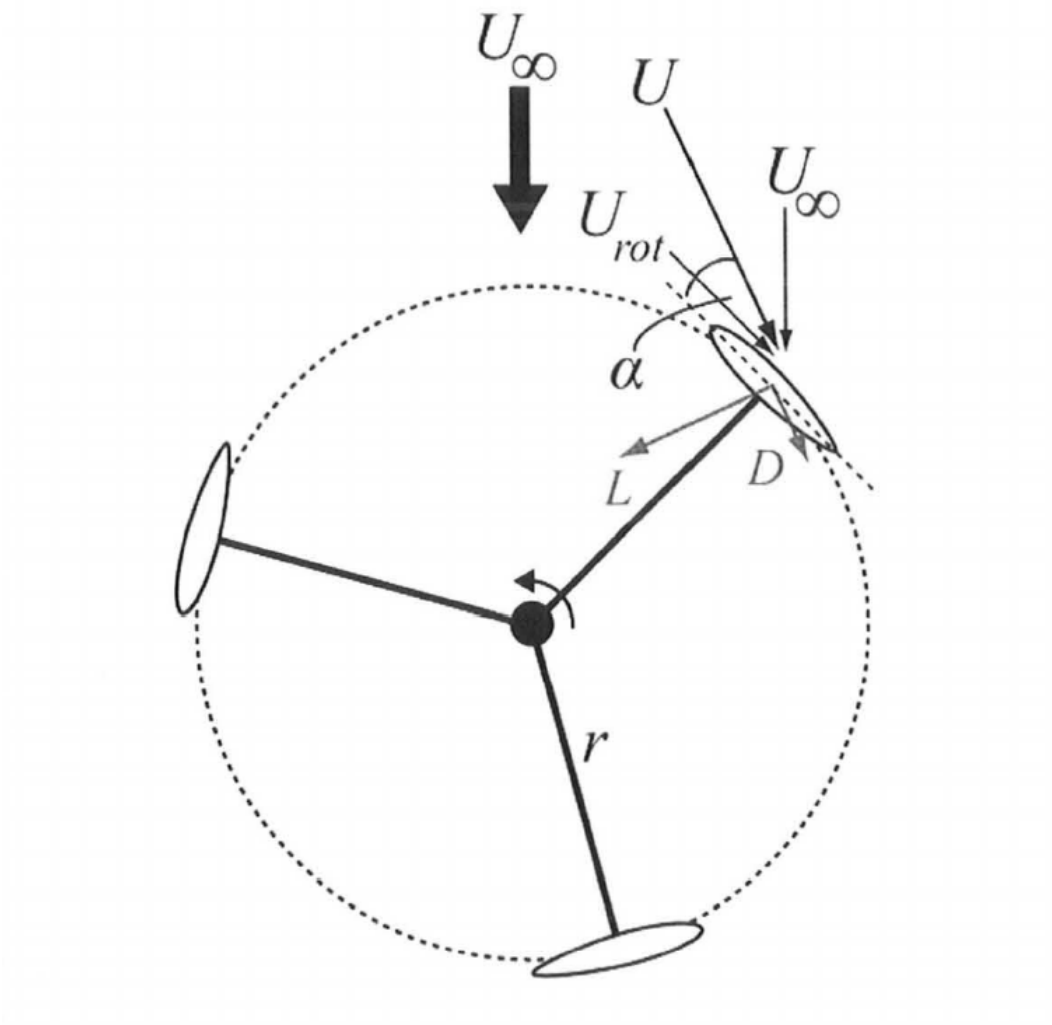

Figure 2: Top view of a straight bladed H type VAWT showing the incoming wind velocity U_∞, turbine blade rotational speed U_{rot}, relative wind speed U, angle of attack α and resulting lift and drag forces. (Fiedler, 2009)

and radial forces all fluctuate with the blade position (θ) as it rotates around the turbine. The net tangential force for a complete rotation of all blades around the turbine determines the aerodynamic power the turbine is capable of extracting from the wind.

Turbine performance is typically characterized by the coefficient of power, a non-dimensional measure of power, defined as:

$$C_p = \frac{P_{out}}{\frac{1}{2}\rho U_\infty^3 S}$$

where P_{out} represents the net aerodynamic power of the turbine, ρ is the air density, S is the swept or projected area of the turbine, and U_∞ is the undisturbed incoming wind speed. The coefficient of power is often plotted versus the tip speed ratio (TSR), which is the ratio of turbine blade speed to incoming wind velocity, and defined as:

$$TSR = \lambda = \frac{U_{rot}}{U_\infty} = \frac{\omega r}{U_\infty}$$

where ω is the rotational rate of the turbine and r is the radius of the turbine. For an H-type vertical axis wind turbine the TSR can also be called the blade speed ratio as every part of the blade is traveling at the same speed due to the turbine geometry.

The geometry of a turbine is classified using three common parameters: the chord to radius ratio (c/r), the turbine aspect ratio (H/D) and the ratio of total blade area to turbine swept area known as the solidity. For an H-type VAWT the solidity is often defined as:

$$\sigma = \frac{NcH}{S} = \frac{Nc}{D}$$

where N is the number of blades, c is the chord length of the blades, H is the

turbine height, and D is the turbine diameter.

The solidity of a VAWT has a large effect on how the relative velocity and angle of attack varies with blade position around the turbine. High solidity turbines tend to operate at a lower rotational speed or TSR. This causes the blades to experience a much higher range of AoAs compared to a low solidity turbine. This is because the AoA is dependent on the magnitude of the incoming wind velocity vector relative to the tangential rotational velocity vector, which is larger for a high solidity turbine. A high solidity turbine can experience angles of attack ranging between $\pm 50^{\circ}$ (McLaren et al., 2012a). Dynamic stall will occur over the blades at these high angles of attack causing the development of vortices that are shed downstream. Shed vortices from the blades on the upstream half of the turbine travel downstream, where they interact with the blades at the back of the turbine and create more complexities in the flow field (Fujisawa & Shibuya, 2001). These dynamic stall effects make it difficult to accurately model a high solidity VAWT.

2.2 Vertical Axis Wind Turbine Modeling

When modeling wind turbine performance, a maximum theoretical turbine efficiency exists. This is known as the Lanchester-Betz-Joukeosky limit, or more commonly, known as the Betz limit (van Kuik, 2007). Betz limit states that, assuming there are no heat transfer or drag losses and the flow is both incompressible and axial, the maximum possible energy that can be extracted

by an actuator disk is 59% of the total kinetic energy available in the incoming flow. Betz limit is based on the principles of mass and momentum conservation for a fluid flowing through an open actuator disk, where an actuator disk is defined as an infinitely thin rotator that extracts power. The fluid is represented by a streamtube (Figure 3) in which the diameter and velocity change with location relative to the actuator disk. This is caused by the disk extracting energy from the fluid resulting in a slower velocity downstream. The slower velocity downstream combined with the physical presence of the disk act as a pressure obstacle to the incoming flow causing flow divergence upstream represented by the smaller streamtube diameter. Betz limit represents the optimal balance between the amount of power being extracted by the disk and the amount of flow that is diverging upstream.

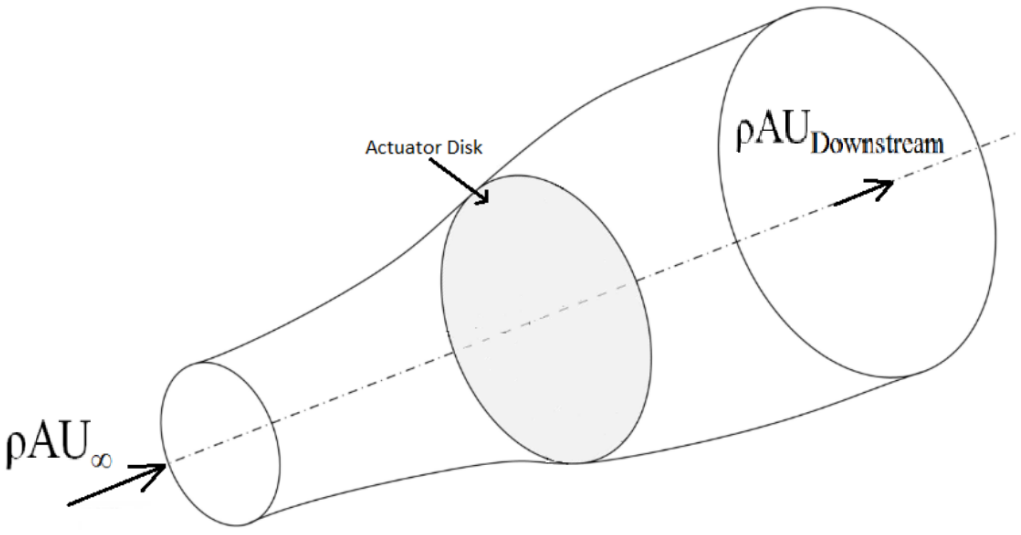

Figure 3: Streamtube of fluid flowing through an actuator disk that extracts power from the fluid, reducing the velocity downstream. This acts as a pressure obstacle to the flow upstream, causing the flow velocity and diameter of the streamtube to change with location.

For a HAWT, this actuator disk theory can be combined with blade element theory and steady state airfoil data to estimate the forces acting on the individual blades and overall power output of the turbine. In this analysis, multiple streamtubes in the form of concentric rings are used to account for the changing TSR with distance away from the turbine centre.

This analysis method was also adapted for use on VAWTs in Strickland (1975) streamtube model and Paraschivoiu (1981, 2002) double multiple streamtube model. Rather than using concentric rings, the multiple streamtubes are vertical slices of the turbine, to account for the changes in the relative wind velocity vector with blade position around the turbine. The double component of the double multiple streamtube model represents the splitting of the turbine into two separate blade passes, an upwind and downwind pass (Figure 4). This is a more accurate representation of a VAWT than using a single streamtube, which assumes that the velocity of the flow does not change within the turbine centre. The streamtube diagram for a double streamtube model (Figure 4) illustrates the potential for the flow to change velocity within the turbine centre and the ability for additional flow divergence around the downwind pass.

The streamtube models for VAWTs still use blade element theory and steady state airfoil data to calculate the forces and power output of the turbine. For low solidity VAWTs, which operate at high TSRs, this type of analysis can give accurate results, but is unable to accurately predict large dynamic stall effects, making it unreliable for high solidity VAWTs operating at low TSRs (McLaren et al., 2012a).

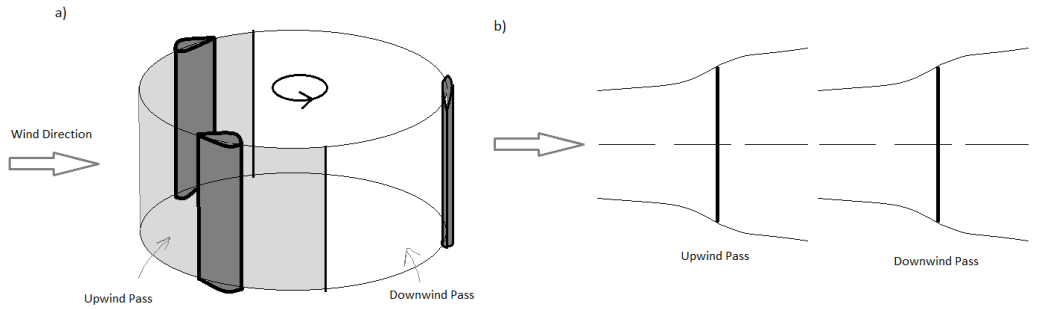

Figure 4: a) VAWT with the location of the upwind and downwind blade passes highlighted b) double streamtube diagram for the VAWT shown in (a)

Simulations using CFD analysis present a better method for modeling high solidity VAWTs because it is able to capture the dynamic stall effects. Initial uses of CFD were limited to 2D simulations. CFD studies by both McLaren et al. (2012a) and Howell et al. (2010) found that 2D simulations consistently over predicted the turbine power output, as they did not account for the flow diverging around the top and bottom of the turbine. McLaren et al. (2012a) incorporated two correction factors, one was a velocity correction factor (κ) that reduced the turbine entrance velocity to account for the vertical flow divergence missing in the 2D simulation. The other factor was a turbine height factor (τ) to account for the potential flow effects of having a turbine blade of finite length. To determine the optimal values for these correction factors, they were iteratively applied to the 2D model and compared to the experimental results until the least error was obtained. Applying the optimal values to the 2D simulation results noticeably improved the accuracy of the predicted power output of the turbine and the TSR in which peak power occurred.

One of the potential flow effects caused by the finite blades is the develop-

ment of tip vortices, an experimental study by Hofemann et al. (2008) used particle image velocimetry to identify the presence of tip vortices developing at the blade tips of a VAWT and tracked how they changed over time. These tip vortices are caused by the pressure difference between the two sides of the blade pushing flow over the top of the blade forming a vortex, just like the tip vortices that develop on an airplane wing. The diversion of this flow to the low pressure side of the blade changes the relative wind and the resulting force output by the tip region of the blades. Both Howell et al. (2010) and Battisti et al. (2011) attributed the improved performance of a 3D simulation to the modeling of tip vortices around the finite blades.

2.3 Three-dimensional CFD Investigations

Despite McLaren et al. (2012a)'s findings, many researchers continue to use 2D simulations to study VAWTs. As such, there are a limited number of studies that have been able to properly study the 3D flow field. This first 3D simulation was done by Howell et al. (2010) for a H-type turbine with 3 blades and a solidity of 1. The simulation was limited in the domain size and grid resolution that could be achieved. The results were briefly compared with a 2D simulation and a wind tunnel experiment to examine the accuracy difference between the 3D and 2D cases. Where the 2D results consistently over predicted the power output, the 3D simulation matched closer to the experiment. As stated in Section 2.2, this improved performance was attributed to modeling the tip vortices found at the blade tips, and showed the importance of a 3D

simulation to accurately model the performance of a high solidity VAWT. Nini et al. (2014) simulated a low solidity 3 bladed H type turbine, and found results similar to Howell et al. (2010), where modeling the finite blade tips improved the accuracy of the simulation results.

Lee & Lim (2015) performed a large 3D CFD study to investigate the impact of multiple turbine geometric parameters including: the thickness ratio, solidity, blade pitch angle, and helical angle. The power coefficients for each case were used to make conclusions for the effect of each parameter. Solidity was found to change the TSR in which peak power occurred, while thickness ratio had negligible effect on performance, contradictory to experimental results (Fiedler & Tullis, 2009). Turbine performance was found to improve with a toe-out blade pitch configuration matching experimental results (Fiedler & Tullis, 2009). The optimal blade pitch angle was found to be at -2° for the given turbine geometry. No clear conclusions were found for the effect of helical angle.

Alaimo et al. (2015) focused solely on how helical blades compared to straight blades on a high solidity VAWT. They first validated their simulations in 2D before moving on to a 3D simulation. Comparing a turbine with helical blades angled at 60° to a straight bladed turbine, they found that at TSRs less than one the helical turbine was more efficient at producing power, while at TSRs greater than one the straight bladed turbine was more efficient. Both turbine geometries had peak power coefficients occur at TSRs greater than one, where the straight bladed geometry was more efficient. The diffu-

sion of shed vortices was also compared for the two turbine configurations. A straight bladed turbine was found to have the vortex regions concentrated near the blade tips where they persisted longer, potentially affecting the performance of the next blade. For the helical blade turbine, the vortex regions were evenly distributed along the blade length and diffused quicker compared to the straight bladed turbine.

Orlandi et al. (2015) used a 3D CFD simulation to test how tilting of the turbines central shaft affected the power output. They tested two turbines: the troposkein turbine geometry from an experimental study by Sandia Laboratory (Akins, 1989), to validate the simulation parameters; and a low solidity 2 bladed H type turbine, to examine the effect of tilting the main axis. They found that tilting the central axis increased the power output of the turbine. This was due to the increase in the turbine projected area and that part of the downwind pass was now interacting with flow undisturbed by the upwind pass. An nearly identical study by Chowdhury et al. (2016) used 3D simulations to test the effect of turbine axis tilt on the same low solidity 2 bladed H type turbine geometry and found similar results for a wider range of tilting angle.

Ghasemian & Nejat (2015) performed a 3D large eddy simulation (LES) to study the aerodynamic noise of a VAWT. Previous literature had shown that a URANS simulation was unable to capture the aero-acoustics properly, which is why an LES approach was used. The noise radiation as a function of TSR and distance from the turbine was analyzed. As expected, it was seen that higher TSRs resulted in higher noise emissions and that the noise level

was found to drop logarithmically with distance away from the turbine.

Lam & Peng (2016) did an extensive study to analyze the near and far wakes of a two-bladed low solidity H type turbine. First they compared a 3D LES to a 3D URANS simulation and found that the URANS simulation performed as well as the LES. Using both 2D and 3D URANS simulations, the wake behind a VAWT was analyzed. The 2D simulation was found to over predict the wake results and not properly capture the asymmetric nature of flow. Similar to McLaren et al. (2012a), Lam & Peng (2016) found that the flow in the vertical direction and other finite blade tip effects were critical to accurately modeling the wakes behind a VAWT.

Using the geometry from McLaren et al. (2012a)'s CFD work, Bhargav et al. (2016) used a 3D URANS simulation to study the impact of fluctuating wind conditions on VAWT performance. The amplitude of the incoming velocity (U_∞) was fluctuated by 10% up to 50%, where a 50% fluctuation was found to have the highest cycle averaged power output. The stronger wind gusts at 50% fluctuation resulted in a larger overall power output, due to the power being a function of the velocity cubed. The optimal fluctuation frequency was found to be 1 Hz for the given geometry and turbine rotation velocity. The vorticity in the vertical direction was also analyzed and the tip vortices were found to effect the vorticity on the blade up to 0.3m away from the tip. This reiterated the importance of using a 3D simulation to accurately model a VAWT.

Recently, two more studies were published that used a 3D simulation of a VAWT. Subramanian et al. (2017) varied the blade profile and number of

blades (solidity) to study their impact on performance. As expected from other studies on these geometric parameters, thicker airfoils and higher solidity turbines performed better at lower TSRs. Vortex development was also analyzed to provide further evidence as to why these results are found for the different geometric parameters. Balduzzi et al. (2017) performed a high resolution 3D URANS simulation of a single bladed turbine to be used as a numerical benchmark for calibrating lower resolution models. In the study, the impact of the finite blade tips on power output was analyzed and a large reduction in output was present near the blade tip.

Several important points arise from this review of literature that have used 3D CFD simulations to investigate VAWTs. Almost all of the studies following McLaren et al. (2012a) have used the SST turbulence model for calculating the turbulent quantities. Many of these studies compared the results between a 2D and 3D simulation, and found that the tip effects associated with the development of tip vortices present in a 3D simulation were critical to accurately model a VAWTs flow field and performance. Studies also found that URANS simulations were just as good as LES for modeling a VAWTs performance and flow field.

2.4 Other Flow Field Investigations

A few studies have investigated the flow field around a VAWT without the use of CFD simulations, by using experimental approaches, or other numerical

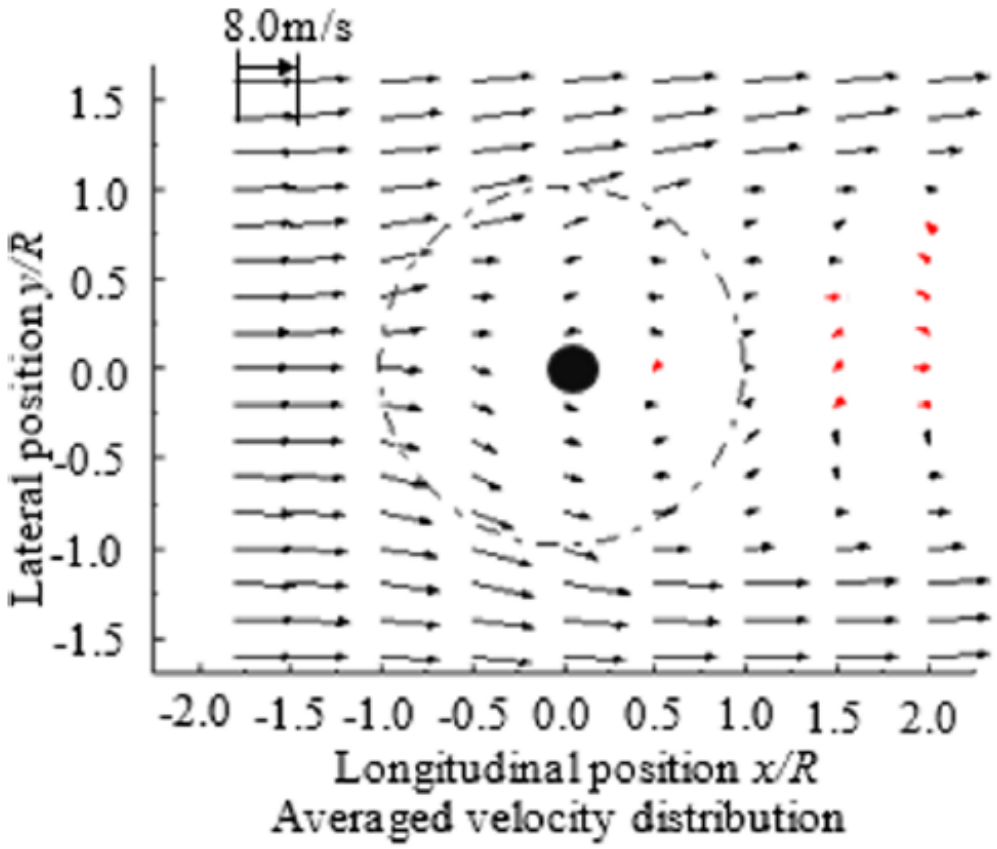

Figure 5: Figure from Li et al. (2016) showing flow velocity vectors on the centre plane of an experimental high solidity H-type VAWT. The velocity vector data was acquired using a laser doppler velocimeter system.

modeling methods. Recent literature by Li et al. (2016, 2017) looked into the flow field using multiple methods. The first paper used an experimental turbine and laser doppler velocimeter system to capture the flow behavior at the centre plane of the turbine (Li et al., 2016). The experimental turbine had an AR of 0.6 and solidity of 0.66. The flow was found to diverge asymmetrically around the sides of the turbine upstream and after entering the turbine a significant decrease in velocity is experienced by the flow (Figure 5). These findings match

experimental results from McLaren (2011) and Brochier et al. (1986), where both found an asymmetric divergence upstream and large velocity deficit in the turbine centre. One contradictory result between McLaren (2011) and Brochier et al. (1986) was the side of the turbine in which the asymmetry upstream flow leaned towards. Li et al. (2016) does not directly indicate the side of the turbine in which more flow is diverging, but inferring from other information it looks to agree with Brochier et al. (1986), the side where the blades are traveling upstream against the approaching flow.

For an in-depth study of the flow field around a VAWT, the complete velocity field surrounding the turbine would be desired. This is difficult to achieve with an experimental approach because acquiring the flow velocity at all these points for an instant in time would require additional instrumentation that has potential to add error to the data. Further, experimental turbines generally have a somewhat fixed geometry, so only a couple specific turbine configurations can be tested at a time. The use of a numerical technique would be more practical to accurately capture the complete flow field surrounding the turbine, and the turbine geometry could be easily altered for comparing a variety of turbine geometries.

The second paper, by Li et al. (2017), used a numerical technique to test the impact of various aspect ratios and solidity of a VAWT on the power performance. Rather than using a CFD analysis method, a 3D potential flow method was used to model the turbine, which is known to inaccurately handle flow separation. Only the torque and power coefficients of the turbine were

used to compare the different test cases. In addition to the solidity of the turbine, this study examined the impact of changing two different aspect ratios: the turbine aspect ratio (H/D) and the rotor aspect ratio (H/c). An increase in the turbine aspect ratio resulted in an increase in the overall turbine power coefficient and the local power coefficient at the turbine centre plane. An observed reduction in the local power coefficient affected a small fraction of the turbine height near the blade tips. As seen with other studies, a change in solidity affected the TSR in which peak power occurred.

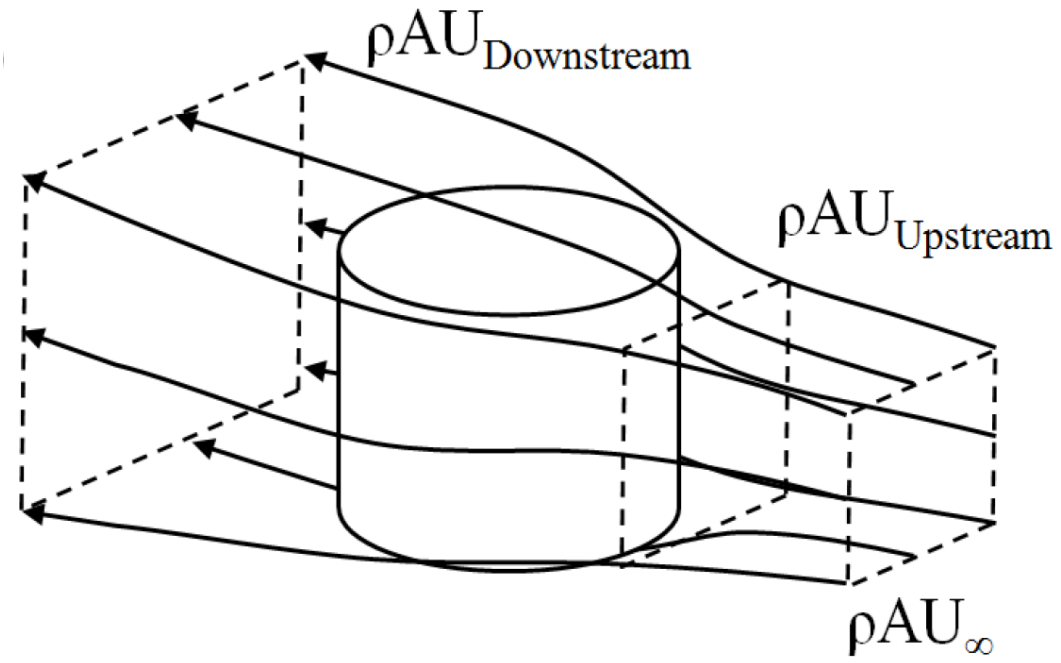

Figure 6: Image showing the flow divergence upstream of a VAWT. The analysis of this flow divergence is the goal of the research presented in this thesis. (McLaren, 2011)

We can see that a wide range of subtopics in the study of VAWTs have been examined to various levels of detail, including: the effect of turbine solidity

and blade thickness, turbine noise emission, development of mid-plane and tip vortices, impacts of tilting the main turbine axis, recovery of downstream wakes, and effects of fluctuating wind conditions. Although the flow divergence around a turbine was recognized very early on in HAWTs as an important determinant of turbine efficiency, there has been almost no research done on the 3D flow divergence around a VAWT. To fill this knowledge gap, this thesis used a 3D URANS simulation to analyze the overall flow divergence upstream and inside of a VAWT (Figure 6) in a detailed manner. Numerical simulations also provided a practical way to examine the impact of how changing the turbine aspect ratio (AR) or TSR of the turbine affected the overall flow divergence and resulting power efficiency.

Chapter 3: Numerical Model

This chapter outlines the numerical modeling approach chosen to study a high solidity VAWT. Based on the literature reviewed a 3D URANS simulation was determined to be the most accurate method for simulating flow around a VAWT. A 3D simulation was chosen since previous studies found that the vertical component of the flow and effect of the finite blade tips were crucial to accurately modeling the flow field around the turbine. A large portion of this work uses the extensive 2D CFD study by McLaren et al. (2012a) and extends it to a 3D domain. The simulations examined here were setup and run by Shawn Armstrong after completing his Master's thesis in 2011.

3.1 Governing Equations

Computational fluid dynamic analysis solve the equations that govern the flow of fluids for a specified set of boundary conditions. For an incompressible and isothermal fluid, these equations are the Navier-Stokes equations and are denoted as follows:

$$\frac{\partial \mathbf{u_i}}{\partial x_i} = 0$$

$$\frac{\partial \mathbf{u_i}}{\partial t} + \mathbf{u_j}\frac{\partial \mathbf{u_i}}{\partial x_j} = \frac{-1}{\rho}\frac{\partial p}{\partial x_i} + \nu\frac{\partial^2 \mathbf{u_i}}{\partial x_j^2}$$

In order to solve the Navier-Stokes equations, the equations are typically time averaged over intervals representative of the turbulent time scale, an ap-

proach commonly known as Reynolds averaging. This separates the turbulent fluctuations and mean flow allowing for an easier solution to the mean flow properties while still keeping the equations time accurate. This averaging is done by decomposing the instantaneous velocity and pressure parameters into an average component and a fluctuating component, as follows:

$$\mathbf{u_i} = \mathbf{U_i} + \mathbf{u_i'}$$

$$p = P + p'$$

Substitution of these components into the governing equations results in the Unsteady Reynolds Averaged Navier-Stokes (URANS) equations, denoted as follows:

$$\frac{\partial \mathbf{U_i}}{\partial x_i} = 0$$

$$\frac{\partial \mathbf{U_i}}{\partial t} + \mathbf{U_j}\frac{\partial \mathbf{U_i}}{\partial x_j} = \frac{-1}{\rho}\frac{\partial p}{\partial x_i} + \nu\frac{\partial^2 \mathbf{U_i}}{\partial x_j^2} - \frac{\partial \overline{\mathbf{u_i'}\mathbf{u_j'}}}{\partial x_j}$$

These appear very similar to the original Navier-Stokes equations with an additional Reynolds stresses term on the right hand side of the momentum equations. This creates a closure problem, as there are no additional equations to solve for the Reynolds stress tensor unknowns. The most common approach used to solve the closure problem is the turbulent viscosity hypothesis, which assumes the Reynolds stress tensor is related to the mean rate-of-strain tensor. This results in the Reynolds stress being replaced by a term similar to that of a viscous stress for a Newtonian fluid, but with a turbulent viscosity term

(ν_T), denoted as follows:

$$\overline{\mathbf{u_i'u_j'}} = \frac{2}{3}k\delta_{ij} - \nu_T\Big(\frac{\partial \mathbf{U_i}}{\partial x_j} + \frac{\partial \mathbf{U_j}}{\partial x_i}\Big)$$

Incorporating this hypothesis into the URANS momentum equations results in the following:

$$\frac{\partial \mathbf{U_i}}{\partial t} + \mathbf{U_j}\frac{\partial \mathbf{U_i}}{\partial x_j} = \frac{-1}{\rho}\frac{\partial}{\partial x_i}\Big(P + \frac{2}{3}\rho k\Big) + \frac{\partial}{\partial x_j}\Big[(\nu + \nu_T)\Big(\frac{\partial \mathbf{U_i}}{\partial x_j} + \frac{\partial \mathbf{U_j}}{\partial x_i}\Big)\Big]$$

The Reynolds stresses have been eliminated, but the turbulent viscosity (ν_T) is still unknown within the momentum equations. A turbulence model is used to solve for the turbulent viscosity providing closure to the equations. Many different turbulence models have been proposed to solve for the turbulent viscosity; the most common have been the two equation approaches such as the k-ϵ (Jones & Launder, 1972) and k-ω (Wilcox, 1993) models and variations of them. Both these models define the turbulent viscosity as follows:

$$\nu_T = C_\mu \frac{k^2}{\epsilon}$$

where C_μ is a constant, k is the turbulent kinetic energy, and ϵ is the rate at which turbulent kinetic energy is dissipated, also known as the turbulent dissipation. These model then use two extra transport equations to solve for the turbulent kinetic energy and the turbulent dissipation. In the case of the k-ϵ model, the second transport equation solves for ϵ directly (Jones &

Launder, 1972). In the k-ω model, the dissipation is solved using a transport equation for ω, which is the specific turbulence dissipation rate and equal to ϵ/k (Wilcox, 1993). The different transport equation used to solve for the turbulent dissipation results in an additional term in the ω transportation equation, changing the models overall performance. The k-ω model has been found to perform well in near wall regions, while the k-ϵ model was found to perform well in the outer part of the boundary layer (Menter, 1994).

3.2 Numerical Modeling Technique

The hybrid finite volume and element method of Ansys CFX was used to perform the numerical simulations of the flow field. This code solves the incompressible URANS equations throughout the domain. The energy equation was not solved for since the flow field was considered to be isothermal.

The governing equations are discretized by a finite-volume scheme and integrated over each control volume. Interpolation of advection terms at the control volume faces was performed using the High Resolution Scheme (barth & Jesperson, 1989) and a second order Backward Euler scheme was used for modeling transient terms. A coupled solver was employed to solve the equations as a single system, utilizing a fully implicit discretization of the equations at each timestep. For each timestep, the equations are first linearized and then solved in an iterative manner using an algebraic multigrid method (Raw, 1996).

The turbulent quantities are solved using a turbulent viscosity model,

specifically the shear stress transport (SST) two equation model developed by Menter (1994). This model combines the two most common two-equation models, the k-ϵ (Jones & Launder, 1972) and k-ω (Wilcox, 1993) models. The SST model blends these two models together, such that in the near wall region k-ω is used, while in the outer part of the boundary layer the model transitions to using the k-ϵ model. In addition, the SST model also accounts for the transport of the turbulent shear stress, which improves the accuracy of flow separation predictions. The resulting equations for the SST turbulence model are denoted as follows:

$$\nu_T = \frac{a_1 k}{max(a_1\omega, SF_2)}$$

$$\frac{\partial k}{\partial t} + \mathbf{U_j}\frac{\partial k}{\partial x_j} = P_k - \beta^\star k\omega + \frac{\partial}{\partial x_j}\Big[(\nu + \sigma_{k3}\nu_T)\frac{\partial k}{\partial x_j}\Big]$$

$$\frac{\partial \omega}{\partial t} + \mathbf{U_j}\frac{\partial \omega}{\partial x_j} = \alpha_3 S^2 - \beta_3\omega^2 + \frac{\partial}{\partial x_j}\Big[(\nu + \sigma_{\omega 3}\nu_T)\frac{\partial \omega}{\partial x_j}\Big] + 2(1-F_1)\sigma_{\omega 2}\frac{1}{\omega}\frac{\partial k}{\partial x_i}\frac{\partial \omega}{\partial x_i}$$

where F_1 is a blend function used to blend the k-ϵ and k-ω models together based on the distance from the nearest wall (y). Coefficients with a 3 subscript represent a summation of the common coefficients between the two models multiplied by their blend fraction. At a solid surface the blend function has a value of one enforcing a purely k-ω model, while far away from any surfaces the blend function has a value of zero resulting in a k-ϵ model.

$$F_1 = tanh\left[\left(min\Big[max(\frac{\sqrt{k}}{\beta^\star\omega y}, \frac{500\nu}{y^2\omega}), \frac{4\sigma_{\omega 2}k}{CD_{k\omega}y^2}\Big]\right)^4\right]$$

$$CD_{k\omega} = max\left(2\rho\frac{1}{\sigma_{\omega 2}\omega}\frac{\partial k}{\partial x_j}\frac{\partial \omega}{\partial x_j}, 1*10^{-10}\right)$$

$$\phi_3 = \phi_1 F_1 + \phi_2(1 - F_1)$$

F_2 is another blend function used to account for the transport of the turbulent shear stress. It has a value of one for boundary layer flows and zero for free shear flows. This function works such that when there is an adverse pressure gradient within the boundary layer, where turbulent production is larger than the turbulent dissipation, the turbulent shear stress becomes proportional to only the turbulent kinetic energy. This greatly improves the model's ability to predict flow separation for adverse pressure gradient flows (Menter, 1994).

$$F_2 = tanh\left[\left(max\left(\frac{\sqrt{k}}{\beta^\star \omega y}, \frac{500\nu}{y^2\omega}\right)\right)^2\right]$$

P_k is the turbulent production due to viscous forces, S is an invariant measure of the strain rate, and S_{ij} is the strain rate tensor. In the turbulent production equation, the second option in the minimum function is a limiter to avoid the excessive generation of turbulence in the vicinity of stagnation points.

$$P_k = min\left(\nu_T S^2, 10\beta^\star k\omega\right)$$

$$S = \sqrt{2S_{ij}S_{ij}}$$

$$S_{ij} = \frac{1}{2}\left(\frac{\partial \mathbf{U_i}}{\partial x_j} + \frac{\partial \mathbf{U_j}}{\partial x_i}\right)$$

Other constants used in the SST turbulence model include:

$$\alpha_1 = \frac{5}{9}, \alpha_2 = 0.44, \beta_1 = \frac{3}{40}, \beta_2 = 0.0828, \beta^\star = \frac{9}{100}$$

$$\sigma_{k1} = 0.85, \sigma_{k2} = 1, \sigma_{\omega 1} = 0.5, \sigma_{\omega 2} = 0.856$$

This blending allows for the use of both model's strengths and diminishes their individual weaknesses. McLaren et al. (2012a) tested a number of different turbulence models and found the SST model to provide the most accurate results for a 2D URANS simulation of a high solidity VAWT. The studies reviewed in Section 2.3 support this finding with the vast majority of them using the SST turbulence model for their 3D URANS simulations of VAWTs.

One limitation of this turbulence model is the lack of transitional modeling as the flow is assumed to be fully turbulent from the start, rather than solving additional transport equations for the intermittency and transitional Reynolds number. Although the flow around a VAWT is transitional, the high AoA cause separation to occur at the leading edge of the blades instead of the separation point being transition dependent along the surface of the blade. This makes high solidity VAWTs have a significantly lower sensitivity to the transitional behaviour of the flow compared to a low solidity VAWT.

3.3 Description of VAWT Model

A straight bladed H type turbine was used for the model. The turbine has 3 straight vertical blades with a NACA 0015 profile. The central shaft and struts of a VAWT are not included in the model, in order to isolate for the blade dynamics. The diameter of the turbine, airfoil shape, and number of

blades are held constant, while the height is varied to change the AR for each test case. The constant diameter at 3m ensures a valid comparison between ARs since changing the diameter would change both the solidity of the turbine and the TSR values between cases. The ARs tested vary from a half to eight with turbine heights of 1.5m and 24m respectively, and all cases have a fixed solidity of 0.43. In addition, a simplified 2D case with no vertical component is simulated and used for comparison. This turbine geometry was chosen to facilitate the comparison with experimental work performed by Bravo et al. (2007) and McLaren et al. (2012b).

A uniform incoming velocity of 12.0 m/s and turbulent intensity of 5% was chosen at the inlet boundary based on the experiments done by Bravo et al. (2007). This gives a $Re_{chord} = 334,000$, which is greater than 210,000 providing results with minimal dependance on the Reynold numbers (Fiedler & Tullis, 2009; McLaren et al., 2012a). A subsonic outlet boundary with relative pressure set at 0 pa was used for the outlet of the domain, and the sides were set as free slip walls so that they did not impose any wall effects on the nearby flow. A symmetry plane was placed at the turbine centre plane such that only half of the turbine is simulated reducing the required overall domain size. The turbine blades were modeled as smooth no-slip surfaces and the uniform velocity at the inlet of 12.0 m/s was used as the initial condition everywhere in the domain.

The inside of the domain is split into two distinct sections: a rotating domain directly surrounding the blades and a stationary domain for the area

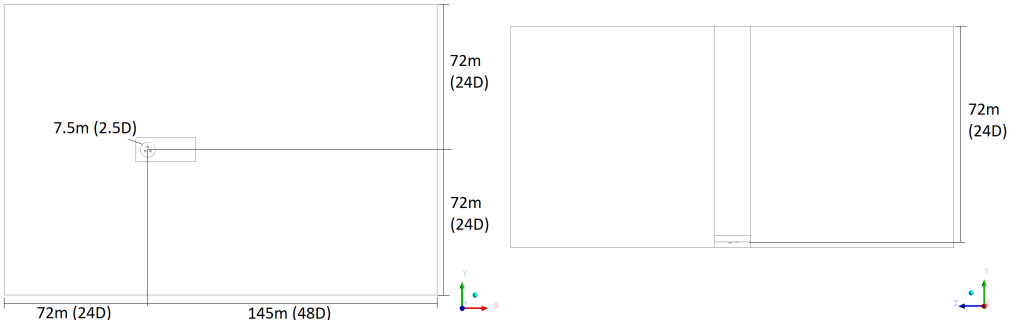

Figure 7: Images showing the dimensions of the simulation domain in both meters and number of turbine diameters. Left image shows a top down view of the domain (XY plane) and right image shows a front view of the domain (YZ plane). Both images are for a turbine with an AR of one.

surrounding the rotating domain. The rotating domain allows for the mesh around the blades to rotate with the turbine, simplifying the mesh calculations within the turbine centre and on the surface of the blades. The rotating domain has a diameter of 7.5 m (2.5 times the diameter of the turbine). The stationary domain has dimensions of: 72m upstream of the turbine, 145m downstream of the turbine, 72m between the turbine centre and each side wall, and 72m between the turbine top and top of the domain as shown in Figure 7. As the height of the turbine is increased to facilitate the change in AR, the height of the domain is increased to ensure a constant of 72m between the turbine top and top of the domain.

A sliding mesh interface with a conservation of mass and momentum flux condition was set at the boundary between the stationary and rotating domains (Blades & Marcum, 2006; Mathur, 1994). This sliding interface works by overlapping the two sub-domains by a single cell to facilitate the transfer of information between local nodes on each respective grid. This transfered

information is than used to interpolate the flux for every timestep iteration at the edge of each domain boundary. This interpolation is only a first order equation and can potentially add numerical error into the flux calculations; to reduce the amount of potential numerical diffusion, the same sized mesh grid is used for both domains at the interface.

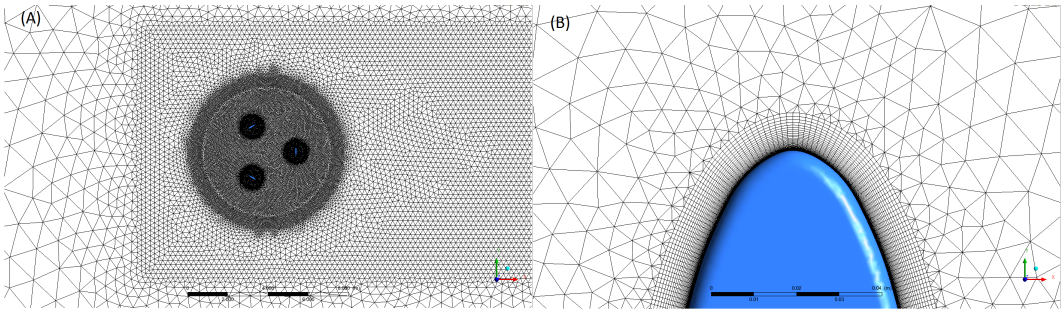

Figure 8: Images of the mesh grids on the XY plane; (A) shows an image of the different levels of mesh refinement in both the stationary and rotating domains, (B) shows a close up of the blade surface where a very fine mesh is used to capture the boundary layer.

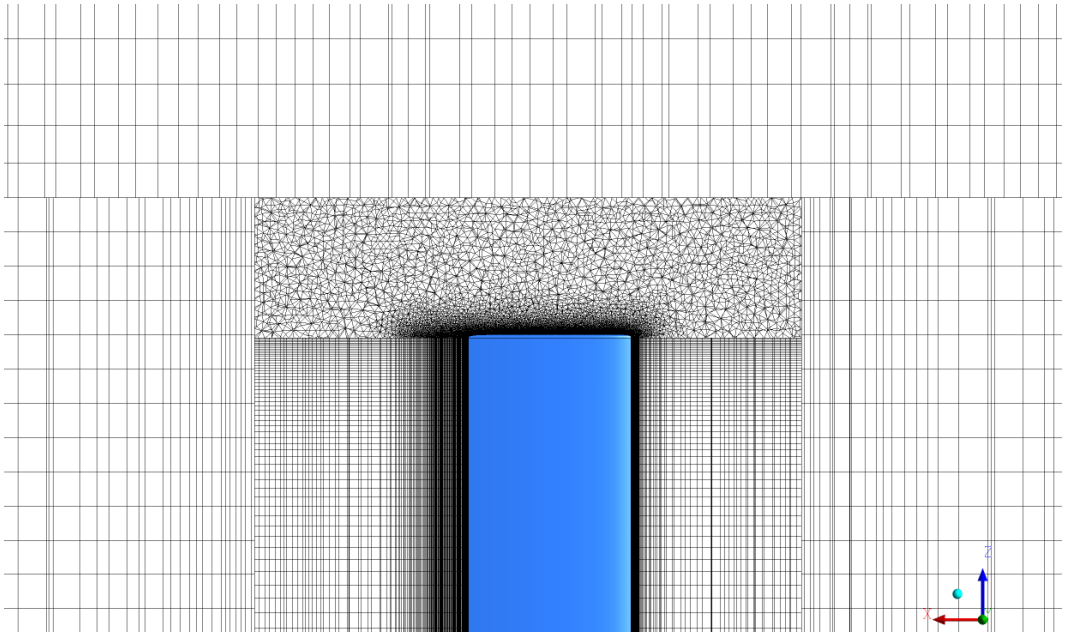

Figure 9: Image showing the mesh grid in the vertical (Z) direction and the fine unstructured mesh around the tip of the blades.

An unstructured triangular mesh was used for most of the domain in the XY plane. Far away from the turbine the mesh is coarse with triangular elements having a size of 2m by 1.75m (base x height). Closer to the turbine and in the wake region downstream, the mesh is refined to an element size of 0.25m by 0.22m. The mesh is further refined to a size of 0.06m by 0.06m within the rotating domain directly around the blades, and extremely refined at the surface of the blades, in order to accurately model the development of the boundary layer. The first node on the blade surface occurred at an average y+ value of 1.5 and a maximum y+ value of 5.4. The width of each rectangular element on the blade surface was 1mm. The mesh in the XY plane was then layered on top of itself in the Z direction to create the three dimensional aspect of the domain, with exception to a fine unstructured triangular mesh located around the blade tips. This unstructured mesh at the blade tips ensures accurate capturing of the finite blade tip effects. In total, the domain for a turbine with an AR of one has 16,044,397 nodes and each blade has a total of 88,638 nodes on its surface. Figure 8 and Figure 9 show the mesh in the XY plane and the mesh in the vertical (Z) direction, respectively.

The selection of the domain size, mesh density, timestep size, and number of initial revolutions for this study was heavily based on the independence testing performed by McLaren (2011) for his 2D URANS simulation of a high solidity VAWT. For the domain size, McLaren (2011) found domain sizes larger than 12.5 turbine diameters by 7 turbine diameters had minimal effect on the peak torque coefficients, by less than 2%, and power coefficients by less than 1.5%. Based on the these findings, the domain sizes for the simulations were chosen

such that they were larger than this threshold. McLaren (2011) optimized the structure and refinement of the mesh grid and tested multiple levels of mesh density for a 2D domain. These results were used for the selection of the mesh structure and density in the XY plane, then stacked in the vertical direction at a similar mesh density to create a 3D domain that would provide results independent of the mesh size.

For the timestep size between each iteration, McLaren (2011) found that timesteps corresponding to less than a 2.5° rotation of the turbine for a given RPM produced results that minimally affected the power coefficients, by less than 1.5%. As such, a timestep size corresponding to a 1° rotation of the turbine was selected to be below this threshold. The number of revolutions required to overcome the initial values was found to be 5 by McLaren (2011) for his 2D study. For 3D simulations a minimum of 10 revolutions were required for the power coefficients to differ by an acceptable level due to the larger 3D domain.

The analysis of the simulation results was done through the use of CFX Post and Octave. The output files for each timestep in CFX were 6-8.5 GB in size and the calculations for the time averaged results were done using Octave to average the data over a full rotation of the turbine in ten degree increments. This meant for each simulation case of a given AR and TSR, csv files with the desired data for each timestep from CFX Post were imported into Octave for calculating the time averaged results. Overall the total amount of data stored in the CFX output files was roughly 3TB.

Chapter 4: Results and Discussion

The results of the 3D CFD simulations are examined here to study the flow divergence around a VAWT. The AR and TSR of the turbine were individually altered between cases to examine how they impacted the flow divergence around the turbine and the resulting power efficiency. All results presented are based on time averaged data for a complete revolution of the turbine.

4.1 Power Coefficients

The power output of the turbine was acquired from integration of the force over the full surface of the blade caused by the surrounding velocity and pressure fields. The net blade force in the tangential direction for a full rotation of the turbine determined the net power output of the turbine. Coefficients of power (Cp) were used to remove the effect of the changing projected area for the different AR cases, ensuring an accurate comparison of the turbine power output. In addition to the turbine ARs simulated, the power coefficients for a 2D simulation (Figure 10) and experimental data from McLaren (2011) (Figure 11) are plotted and compared to the 3D simulation results.

Changes in AR have a significant effect on the power coefficients (Figure 10). There is a steady increase in peak power coefficient with increasing AR, with a 20% increase in peak coefficient between ARs a half and eight. The peak power coefficient of 0.38 for the 2D simulation was approximately 8%

higher than the AR eight case. Each power curve in Figure 10 has the peak power coefficient occur near the same TSR of 1.86. At higher TSR values the incremental differences observed with AR change is larger compared to at low TSRs. Based on the automatic lines created by excel between points, the optimal TSR was observed to slightly decrease for lower AR turbines, but more simulations closer to the TSR of 1.86 would need to be run to confirm any conclusions about the AR impact on peak TSR.

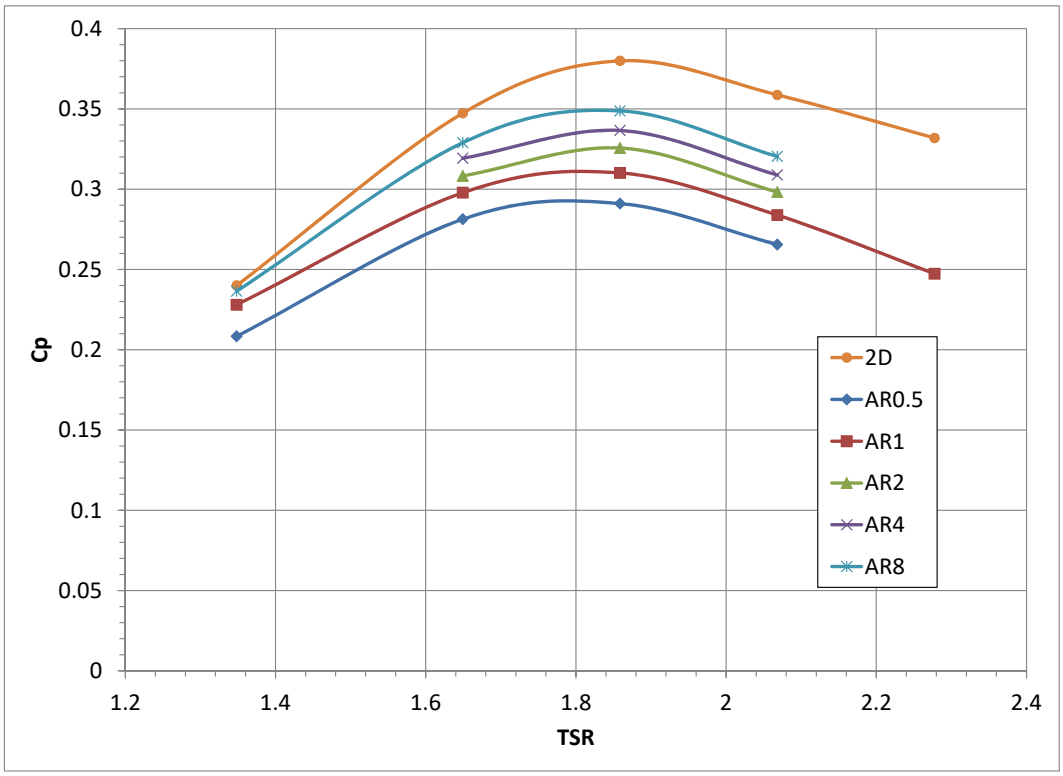

Figure 10: Fluctuation of power coefficient as a function of TSR. Results from the 2D simulation are shown in addition to all the 3D simulation cases.

Figure 11 displays a comparison between the 3D simulations from this thesis and experimental data from McLaren (2011)'s experimental H-type VAWT,

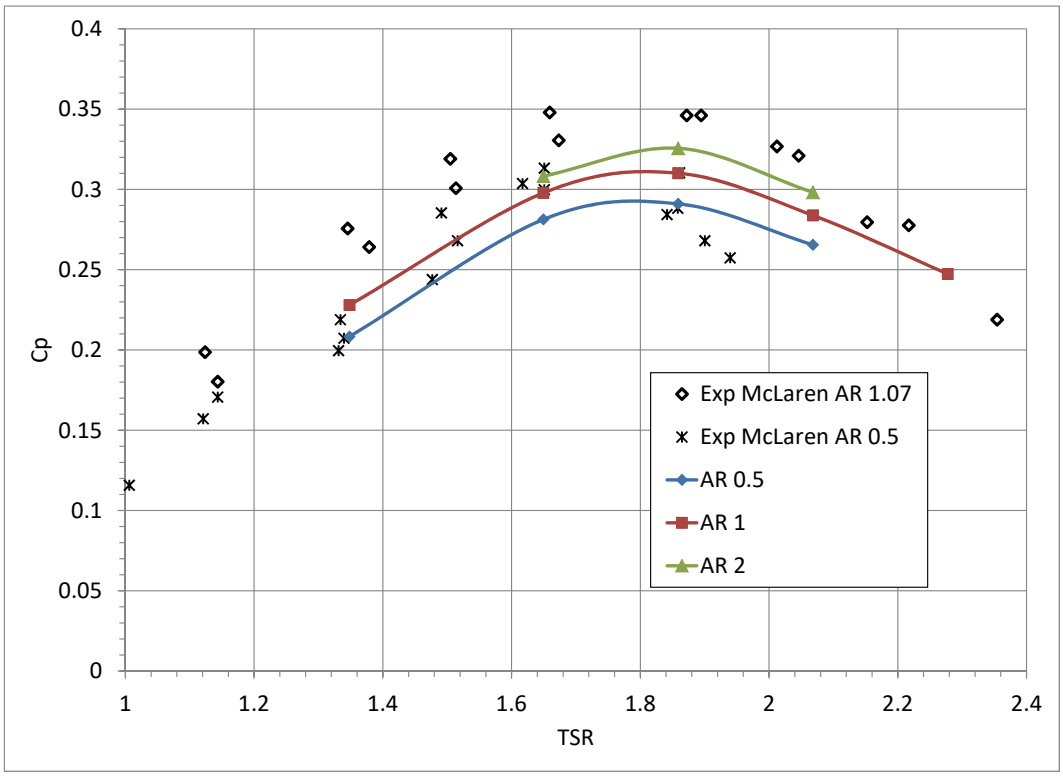

Figure 11: Fluctuation of power coefficient as a function of TSR for simulated ARs one and a half compared to experimental data from McLaren (2011).

which was tested with ARs of 0.5 and 1.07. The experimental VAWT had 3 blades of NACA 0015 profile and a diameter of 2.8m, which is similar to the geometry used in this study. McLaren's AR 1.07 turbine was slightly larger than the AR one case simulated in this study, but based on the results seen in Figure 10, a 0.07 difference in AR is not expected to have a large effect on the power coefficients. The results of this study and McLaren (2011)'s experimental results match well with one another. The peak power coefficients for this study versus McLaren (2011) are 0.29 and 0.31 for the AR half case, and 0.31 and 0.35 for the AR one case. In both cases, McLaren (2011)'s experimental

results are higher than the simulated resulted, which may be attributed to the experimental turbine configuration.

The experimental results were based on a ground mounted turbine in a open wind tunnel with test section dimensions of 8m wide and 7.6m high. The restrictions of the wind tunnel size, especially the closeness of the floor to the bottom of the turbine, could have prevented some flow from naturally diverging around it resulting in a higher power output. This would have had a greater effect on the AR 1.07 turbine as the blades would be much closer to the floor making it somewhat like a symmetry plane, resulting in a turbine that was effectively closer to an AR of two. The floor is not exactly a symmetry plane though, as there would be a boundary layer present significantly impacting the flow velocities near it. The other experimental configuration that could have caused an increase in the power output was the location of the infinitely far upstream velocity measurement not being far enough upstream. McLaren (2011) measured the infinitely far upstream flow velocity halfway between the plenum exit and the experimental turbine potentially missing flow divergence that occurred farther upstream.

4.1.1 Mclaren's Correction Factors

McLaren (2011) applied two correction factors to his 2D CFD simulation in an attempt to make up for the missing 3D effects, as discussed in Section 2.2. The two factors were a velocity correction factor, κ, and a height correction factor, τ. The velocity correction factor altered the infinitely far upstream

velocity to account for the additional flow divergence that was expected to occur for a 3D turbine. From the formulas below one can see that this factor impacts both the TSR and the power coefficients effectively moving the 2D power curve both vertically and horizontally.

$$U_{eff} = U_{\inf}\kappa, \lambda_{eff} = \frac{\lambda}{\kappa}$$
$$C_{Feff} = \frac{C_F}{\kappa^2}, C_{Peff} = \frac{C_P}{\kappa^3}$$

The height correction factor altered the effective height of the turbine to account for the finite length of the blades and the 3D flow affects that occur around their tips. Unlike κ, this factor only effects the power coefficients and does not impact the TSRs as shown below.

$$H_{eff} = H\tau$$
$$C_{Feff} = \frac{C_F}{\kappa^2 * \tau}, C_{Peff} = \frac{C_P}{\kappa^3 * \tau}$$

These factors using McLaren's values were applied to the 2D results for this geometry and compared to the actually 3D simulation results to better understand their relevance (Figure 12). For the results in this study, applying McLaren's values reduced the 2D results to be significantly lower and to the left of the 3D simulation results. Applying each factor individually, κ had a stronger impact on the curve location pushing it too far left and below the 3D

results, while τ moved it down to a magnitude closer to the 3D results but with a slightly off curve shape. McLaren's values for the correction factors were chosen to be an optimal fit between his experimental and 2D results, and as seen in Figure 12 are not able to accurately transform the 2D simulation results here to match those of the 3D simulation results. This shows that although the correction factors are effective at shifting the power curve to a desired location, they must be properly fitted for the specific scenario.

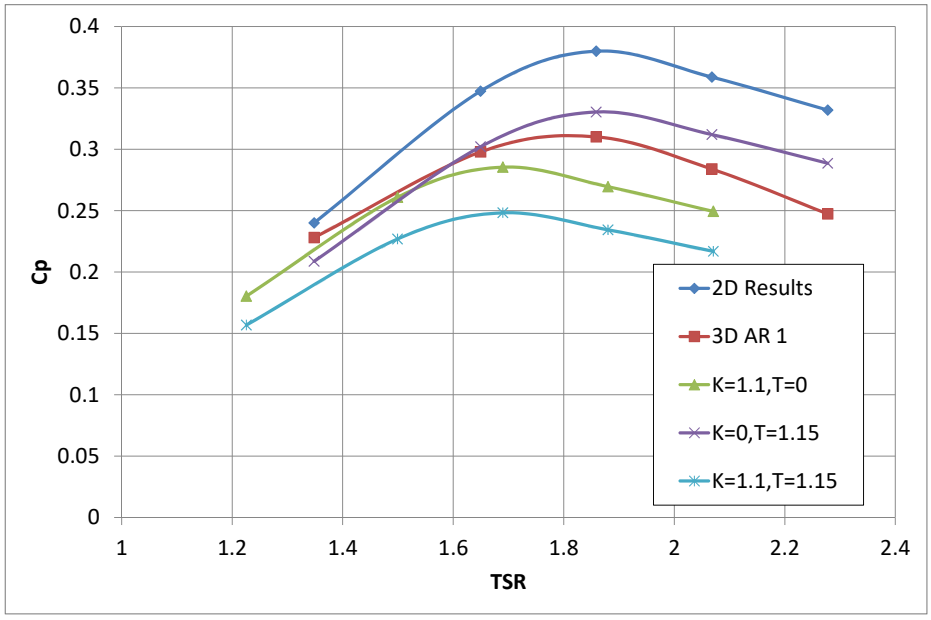

Figure 12: Effectiveness of McLaren's correction factors on the 2D results compared to the actually simulated 3D simulation results. The values used for kappa and tau were 1.1 and 1.15 respectively, based on McLaren (2011).

The correction factors do present a good starting point for studying the flow divergence and 3D flow effects that occur around a VAWT. By analyzing

the flow field to understand if the physical theory behind each factor is correct, it can show how relevant they are to the actual physics of the flow around a 3D VAWT.

4.2 Results for AR Change at Peak Power TSR

All results presented in this subsection are for the turbine rotating at its optimal TSR for producing power. As found in Figure 10, the optimal TSR was mostly unaffected by the change in AR and as such all results presented are for a TSR of 1.86. Using a constant TSR while changing the AR of the turbine allows for the analysis of how AR impacts the flow divergence around the turbine. The flow divergence is broken down into two subsections, one for the divergence occurring far upstream, and another for the flow diverging immediately before the turbine entrance.

4.2.1 Far Field Upstream Flow Divergence

Planes the same size as the turbines projected area in the YZ plane were placed at a range of locations upstream of the turbine (Figure 13). The average streamwise velocity calculated for each plane was then used to quantify the fraction of approaching flow that diverged around the turbine and where it diverged. Figure 14 shows this drop in velocity as flow approaches the turbine.

Far upstream, greater than two diameters, the slowing of the velocity is

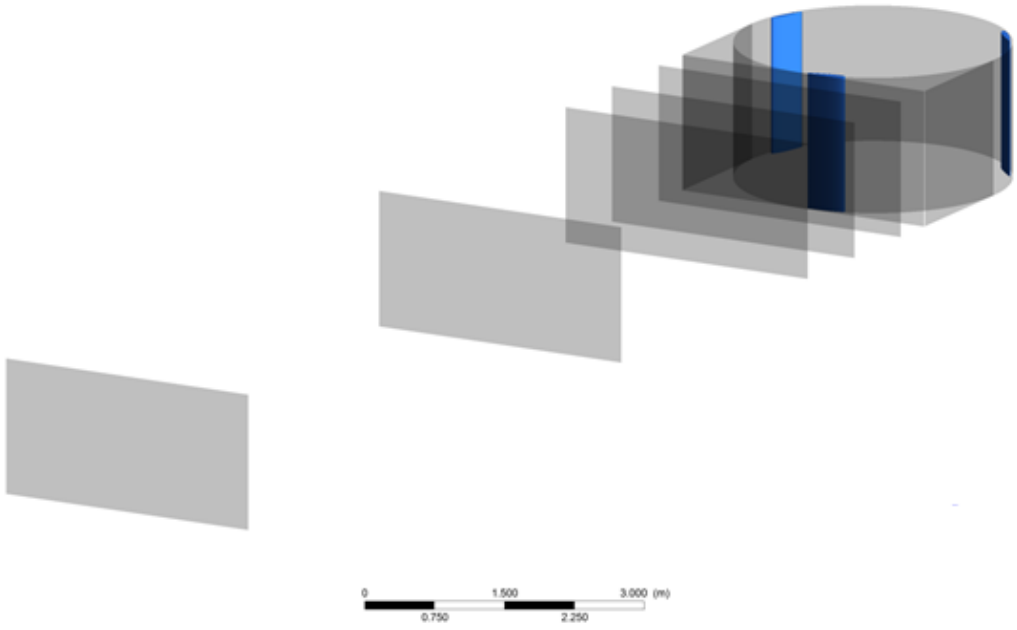

Figure 13: Image showing the turbine with planes upstream used to capture the upstream flow divergence. Each plane has the same area as the turbines projected area in the YZ plane. The turbine in this image has an AR of one, but due to the symmetry boundary at the turbine centre only half of the height is simulated.

gradual until it reaches the near field region, less than two diameters, where it becomes much more severe. The curves in Figure 14 show that more flow diverged around higher AR turbines and that it started to occur further upstream. The average velocity one turbine radius upstream for the AR eight case is 12% less than for an AR of a half. With noticeable divergence occurring farther than two turbine diameters upstream (six meters), this indicates that McLaren's measurement location of the infinitely far upstream velocity on the experimental turbine would have missed some of the initial divergence. Additionally, the 2D results matched closely with the AR eight case, which indicates that turbines of AR eight and greater would have far upstream di-

vergence similar to the 2D results.

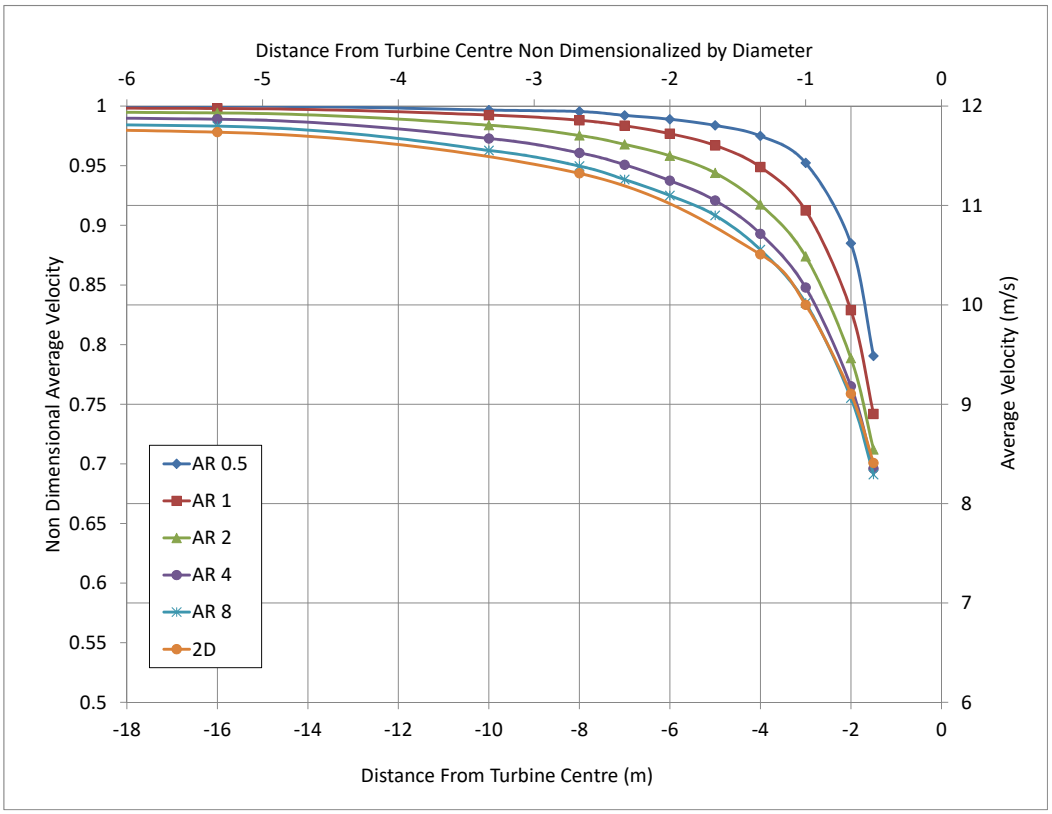

Figure 14: Change of average streamwise velocity with distance from the turbine centre representing the amount of upstream flow divergence. Velocities are shown for far away (20m) to one radius (1.5m) upstream of the turbine centre which is the first contact point for the upwind pass. Results for ARs a half to eight as well as the 2D case are shown.

The 2D simulation results are compared with the exact solution for the inviscid flow around a 2D cylinder to see if it could be used to predict the upstream flow divergence (Figure 15). The upstream divergence was found to be independent of the circulation value for a rotating 2D cylinder, so this comparison does not clarify if the cylinder is rotating or what the circulation value is, more details can be found in Appendix A. Far upstream of the obstacles, the two results have a similar shape but differ in magnitude with a 250% and

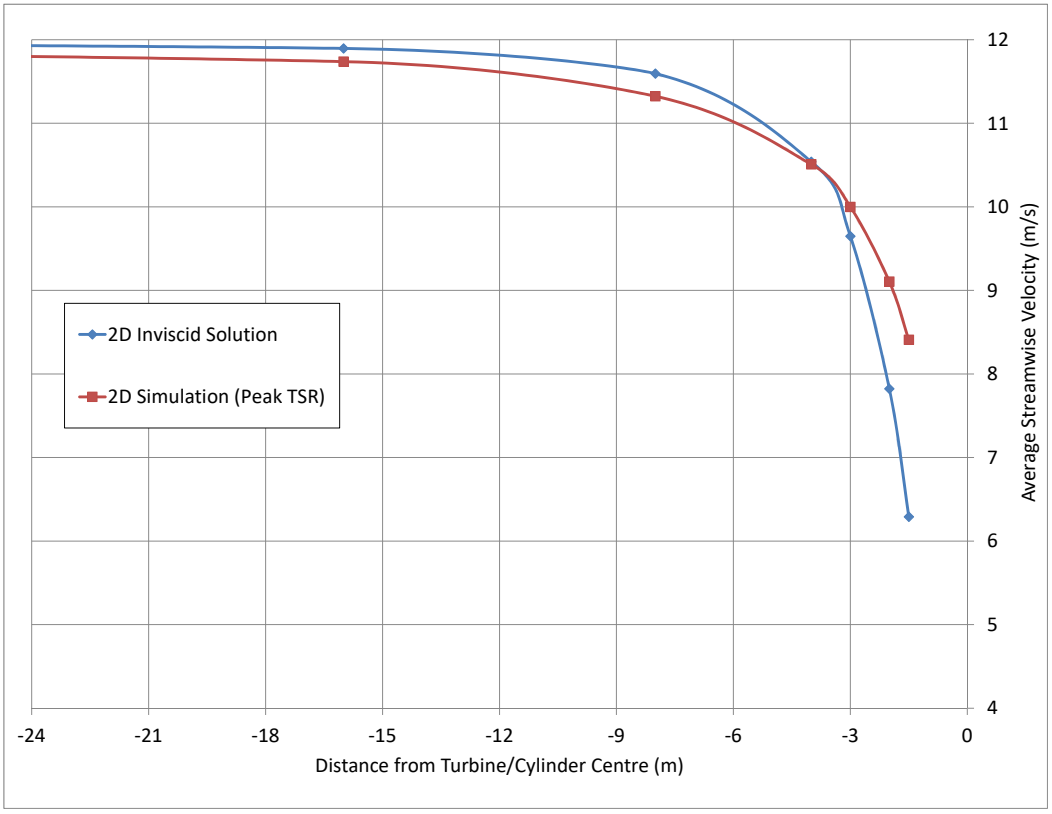

Figure 15: Change of average streamwise velocity with distance from the turbine centre comparing the 2D simulation results to the exact solution for the inviscid flow around a 2D cylinder.

166% increase in divergence for the 2D VAWT, 16 and 8 meters upstream of the turbine respectively. Once less than two diameters (six meters) from the obstacle centre, the inviscid solution drops much lower than the 2D VAWT, as it converges toward a value of zero. This showed that overall the exact solution for the inviscid flow around a cylinder is not an accurate representation of the upstream flow divergence experienced by a VAWT.

4.2.2 Near Field Upstream Flow Divergence

To depict this near field divergence in greater detail, the plane closest to the turbine, at 1.05 radius upstream, was selected and examined for the localized direction and magnitude of the velocities. These plots are than compared for the different AR cases with Figure 16 showing ARs one, two, and four. All three images look extremely similar with a bullseye-like pattern created by the streamwise velocity contours. In addition, the centre of the flow deceleration is displaced by roughly 0.2 m toward the side of the turbine with upstream-oriented blade rotation. This result shows the asymmetric nature of the flow around a VAWT as explained in Section 2.4 and agrees with Brochier et al. (1986) on which side of the turbine has more flow divergence.

For ARs two and four shown in Figure 16 an almost 2D flow region where the velocities stay constant with changes in height is seen far away from the blade tips. In this 2D flow region the crosswind velocities are predominately horizontal pointing toward the sides of the turbine and the streamwise velocity contours do not change with turbine height. Once within one radius (1.5m) of the blade tips the flow becomes 3D with crosswind velocity vectors transitioning to be more vertically orientated and streamwise velocities increasing with height. Since the full height of the AR one turbine is within one radius of the blade tips, no 2D region is seen to develop. The 3D tip region is very similar between all three turbine ARs, such that the higher AR turbines look like extended versions of the smaller AR turbines.

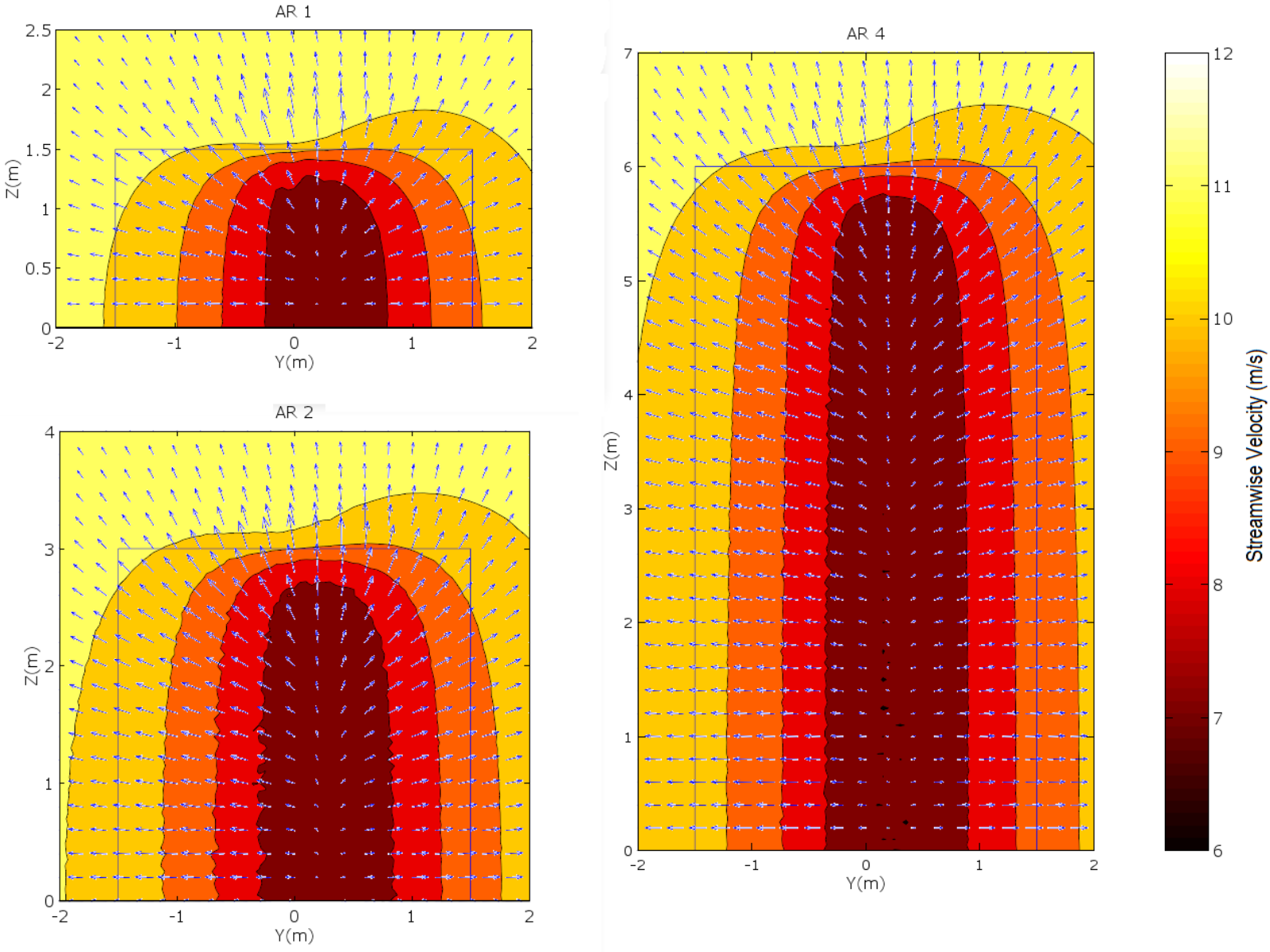

Figure 16: Combination of a contour and vector plots showing the flow field one radius plus one airfoil thickness upstream of the turbine centre. The contours displays streamwise velocity and the vectors show crosswind velocity. Velocities on the colour bar are in m/s and the black lines forming a rectangular box represents the turbines projected area. The turbine rotation is such that on the readers left side of the image there is a blade moving downstream with the streamwise velocity and the right side has a blade moving upstream against the streamwise velocity. Three plots are shown for turbine ARs one, two, and four.

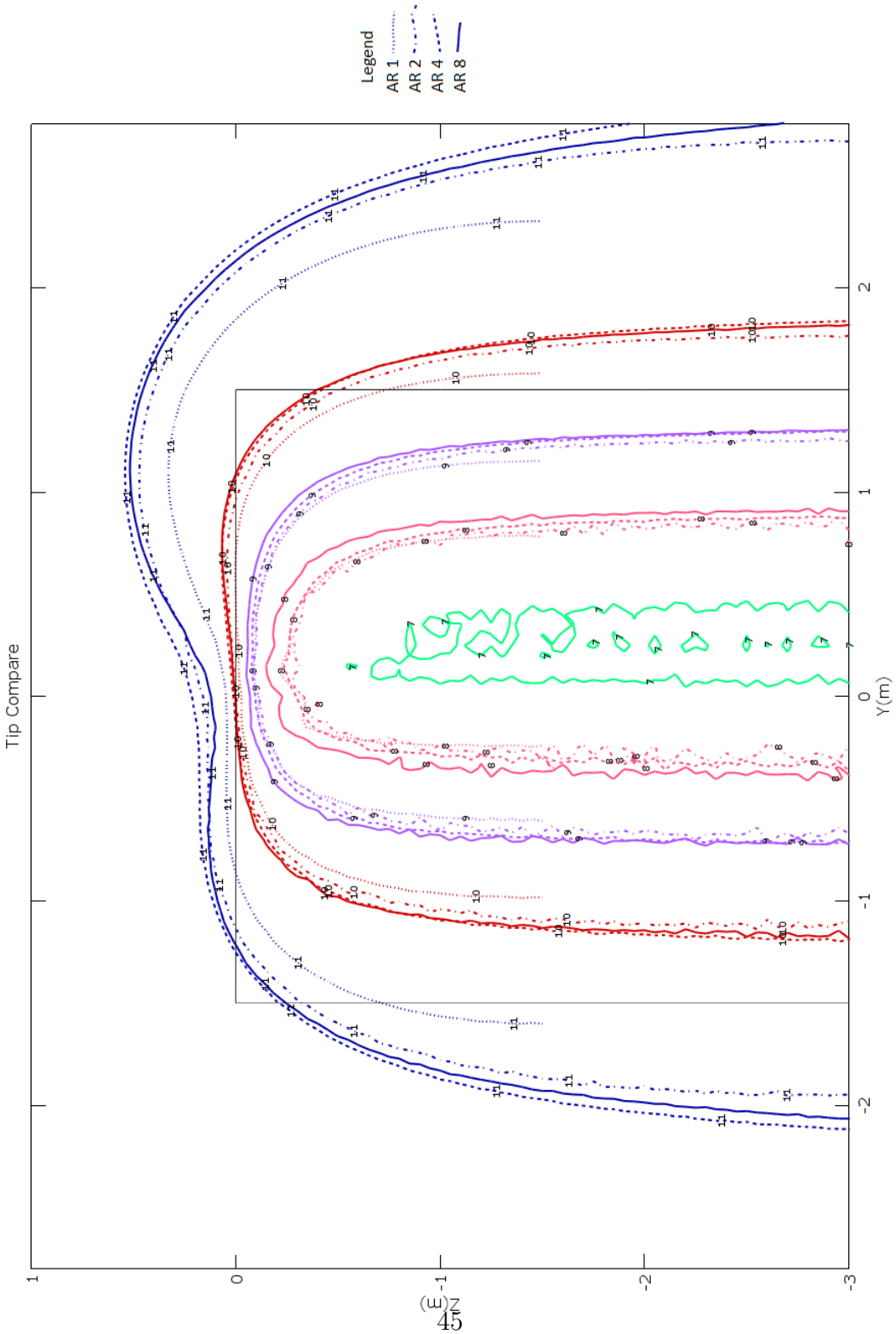

Figure 17: Overlap plot of the streamwise velocity contour lines for ARs 1 to 8. The Z value of zero represents the height at the blade tips and negative values represent moving inwards toward the turbine centre.

The streamwise velocity contours for turbine ARs of one, two, four, and eight are overlapped to see exactly how similar the 3D tip regions is in Figure 17. The plot showed that the contour lines are almost an exact match for turbine ARs of two and higher, with only a slight broadening of the contours as the AR is increased. Higher streamwise velocity deceleration is also seen for the AR eight case, as it is the only one with a 7 m/s contour line at the centre of the turbine (the solid green line). This result indicates that for turbine ARs greater than one the 3D tip region does not increase in size, affecting a relatively fixed distance from the blade tips.

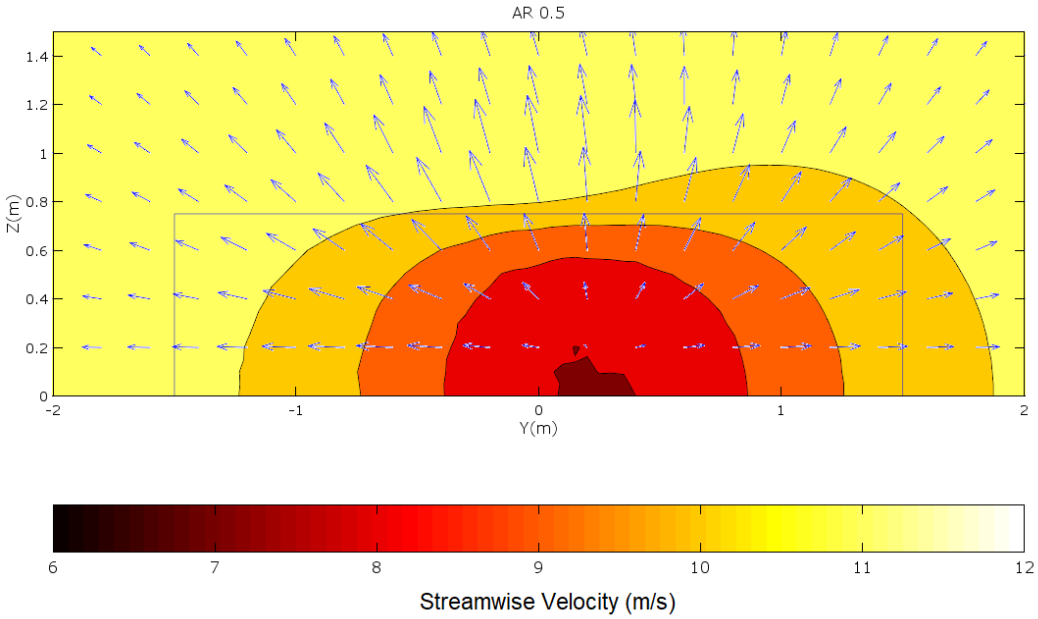

Figure 18: Same plot as Figure 16 but for a turbine AR of a half.

Figure 18 shows an identical contour plot to those in Figure 16, but for a turbine AR of a half. The half AR turbine has noticeably higher streamwise velocities within the turbines projected area. This supports the divergence

results seen in the far field region where the half AR case had a significantly lower velocity reduction upstream. Similar to the AR one case, the half AR turbine also has no 2D region as the full height of the turbine is very close to the blade tips.

Once the flow reached one turbine radius upstream, the central flow comes into contact with the upwind pass of the blades, at a value of y=0. At this point though, the flow is still able to diverge around the turbine without entering the upwind blade pass. To analyze this divergence, a virtual box composed of planes was created around the upstream half of the turbine (Figure 19). All planes of this box were labeled and analyzed individually due to the asymmetric nature of the flow. Figure 20 shows how the average velocity through each of these planes changed with AR, while Table 1 summarizes the upstream flow divergence results in terms of volume flow rates.

Figure 20 shows that the flow continues to diverge immediately in front of the upwind pass by going over the top or around the sides of the turbine. Similar to further upstream, a higher AR turbine has more flow diverge around it, which results in a lower average entrance velocity for the upwind pass of the turbine. The curves have an asymptotic behaviour with ARs four and eight having almost identical values and AR a half having the largest difference. The asymmetric nature of the flow is also seen here with a higher flow velocity around the positive V side of the turbine, matching the results seen in Figure 16's contour plots and those found experimentally by Brochier et al. (1986).

Table 1 shows a summary of the total upstream flow divergence results for

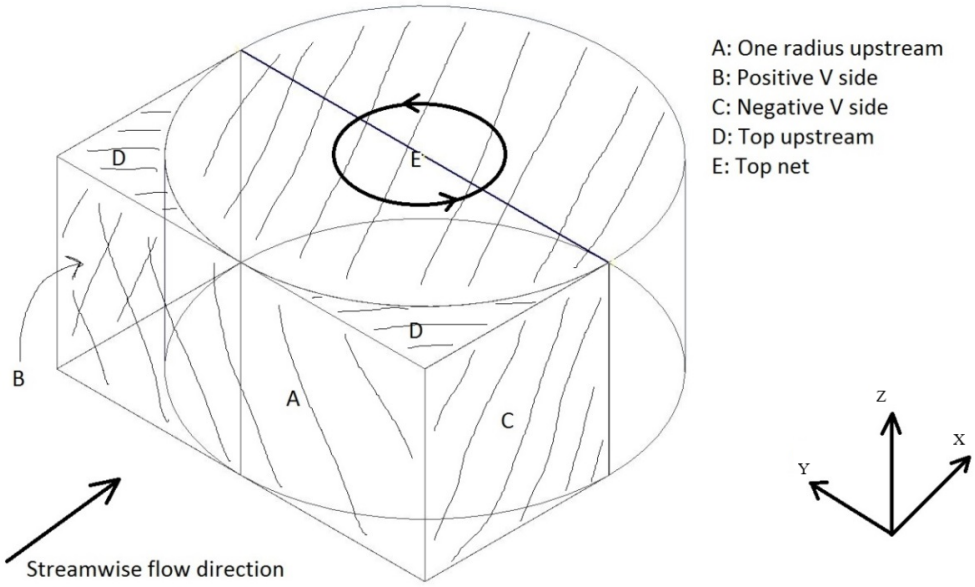

Figure 19: Depiction of planes surrounding the upwind half of the turbine with labels showing each planes' name. Arrows indicating the direction that incoming wind approaches and the rotational direction of turbine.

all AR cases and the 2D simulation. Unlike the figures shown in this section, the volume flow rates are used in the table rather than the velocities. This means that the area change with AR affects the volume flow rates and the percent change between planes is required to properly compare the different AR cases. As found throughout this section, higher AR turbines have more flow diverge around them upstream. There is minimal difference in the overall divergence between the AR four and eight cases, and they both have percentages close to the 2D results. For the near field divergence a greater fraction of the flow diverges around the sides of the turbine as the AR is increased, which was not visible in the velocity results in Figure 20 due to the impact of the area changing for the side planes, but not the top.

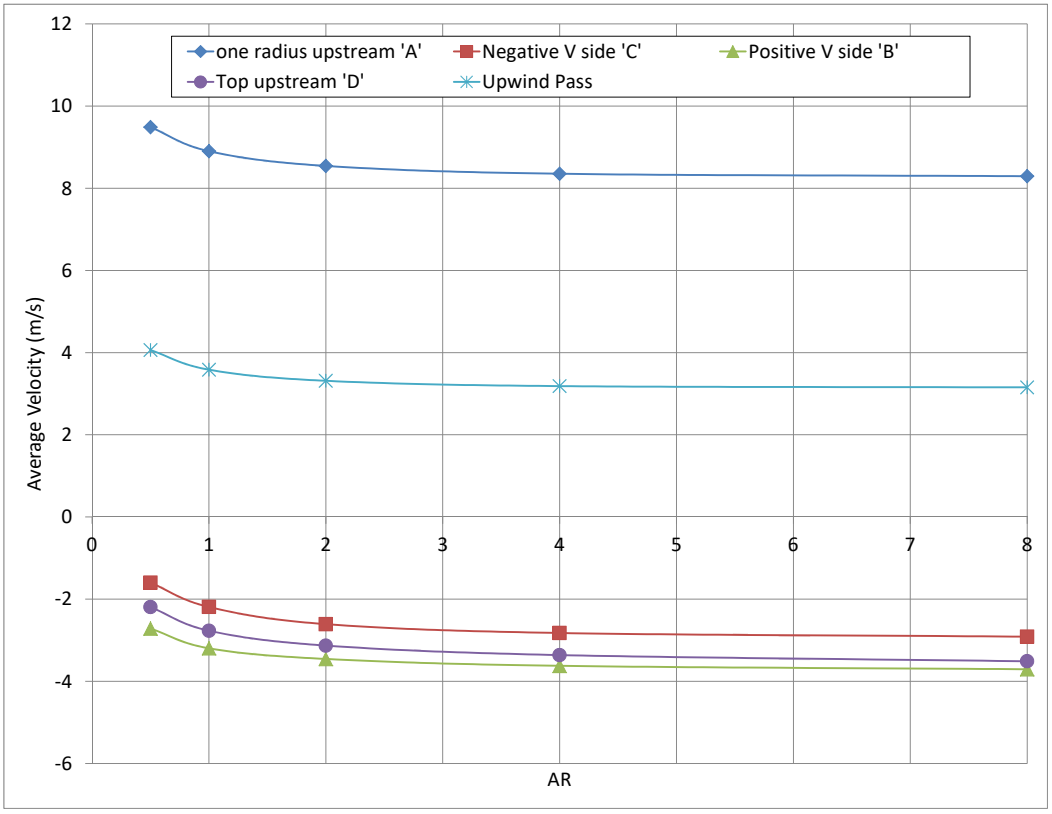

Figure 20: Immediate flow divergence as a function of AR for the different planes shown in Figure 13. Negative values for velocity indicate that flow is diverging around the turbine and upwind pass represents the flow going through the upwind blade pass of the turbine.

The critical result found from this flow divergence analysis is that a smaller AR turbine has a markedly higher velocity entering the upwind blade pass. This is the opposite of what was expected and conflicts with the idea behind McLaren's velocity correction factor κ, showing that it is not a good physical representation of the real flow physics. This result also indicates that a smaller AR turbine should theoretically be more efficient at producing power for a given incoming wind speed, even though the power curves in Section 4.1 have already shown the opposite result.

Table 1: Change of volume flow rates with AR for different planes upstream. All AR volume flow rate results are based on a half area turbine due to the use of a symmetry plane in the model. Volume flow rate results for the 2D case is based on a nominal height of 10mm. For a visual image of the different planes relative to a turbine refer to Figure 19.

Label	Defined Planes	AR					
		0.5	1	2	4	8	2D
	Infinitely far Upstream (m^3/s)	27.0	54.0	108.0	216.0	432.0	0.36
A	One Radius Upstream (m^3/s)	21.3	40.1	76.9	150.3	298.5	0.25
B	Positive V side (m^3/s)	3.1	7.2	15.5	32.6	66.7	0.06
C	Negative V side (m^3/s)	1.8	4.9	11.7	25.4	52.4	0.04
D	Top upstream (m^3/s)	2.1	2.7	3.0	3.2	3.4	0.00
	Upwind pass (m^3/s)	14.2	25.0	46.0	88.1	173.7	0.15
	Percent of infinite upstream entering plane 1R upstream	78.9%	74.1%	71.2%	69.6%	69.1%	70.1%
	Percent of infinite upstream entering the Upwind pass	52.5%	46.2%	42.6%	40.8%	40.2%	41.3%
	Percent of 1R upstream exiting through Positive V side	14.3%	18.0%	20.2%	21.7%	22.3%	22.5%
	Percent of 1R upstream exiting through Negative V side	8.4%	12.3%	15.3%	16.9%	17.6%	17.8%
	Percent of 1R upstream exiting through Top Upstream	9.92%	6.67%	3.93%	2.16%	1.14%	0.0%

4.2.3 Tip Effects

Sections 4.1 and 4.2.2 showed contradictory results, with smaller AR turbines having a higher upwind pass entrance velocity; however, analysis of the power coefficients showed that they are less efficient compared to larger AR turbines. This discrepancy may be due to the effect of the tips of the finite length blades, which have been found to cause a reduction in power output in the near tip region (Balduzzi et al., 2017; Li et al., 2017) and were the basis for McLaren's τ correction factor. This power reduction at the blade tips is often cited to be a consequence of the tip vortices that develop around the end of an aerofoil as discussed in Section 2.2.

Figure 21 shows the instantaneous flow on the mid plane with a blade at a position of $\theta = 90$, where both the vertical divergence of the flow on this plane and the tip vortices can be seen. There are only minor differences visible in the flow field, the main one being the angle of the flow as it approaches the turbine. For the smaller ARs (a half and one) the flow approaching the blade tips has a smaller vertical component compared to the larger AR turbines. The second difference is the behaviour of the flow on the inner side of the blade, where for smaller ARs the flow appears to travel farther into the centre of the turbine area before being pushed upwards again.

To analyze the impact of these tip effects on the turbine performance, local torque profiles (torque on an individual blade as a function of rotation angle) and local power coefficient were calculated for 1mm thick slices of the turbine

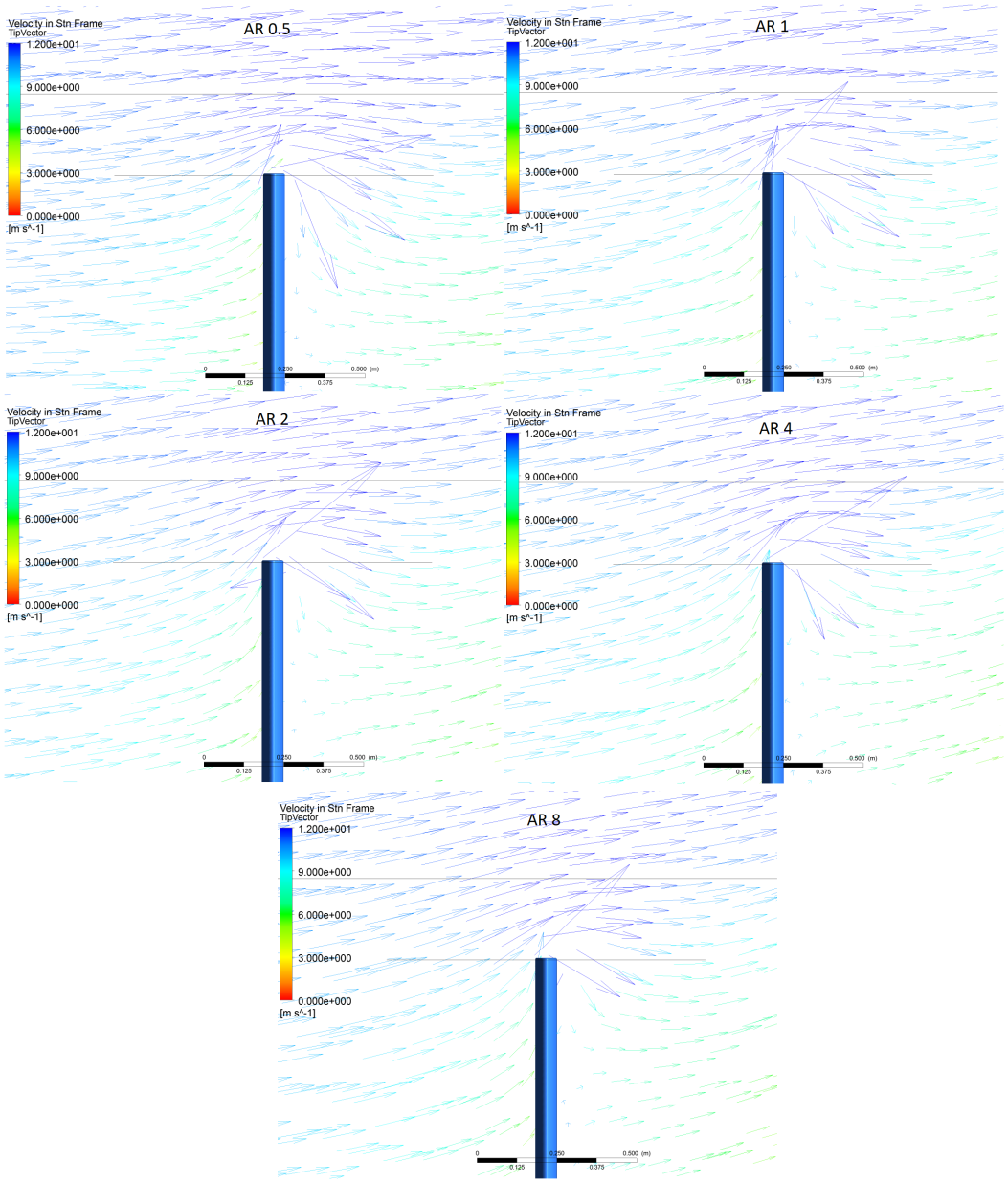

Figure 21: Vector plots showing the flow field on the mid plane of the turbine when a blade is at a position of $\theta = 90$, highlight the tip vortices. All AR cases tested are shown and vector contours are consistent so that velocities can be compared directly.

at different heights. Figure 22 shows the torque profiles for each of these slices as a function of distance from the blade tips for all ARs. The centre line torque

profiles have a similar shape to McLaren et al. (2012a), with the vast majority of the torque generated by the upwind pass and very little torque produced by the downwind pass. Once within 0.7m of the blade tip, the torque produced by the upwind pass starts to decrease while keeping the same overall shape. At 0.1m from the tip, the peak torque output of the upwind pass is approximately half of the centre line peak torque. At 0.05m away from the tip the torque output is approximately 10% of the centre line peak and at the slice directly at the tip there is a large negative torque output.

Directly comparing the different ARs in Figure 23, shows that for the upwind pass the same overall trends are seen for each AR. There is a slightly larger overall torque output seen for the smaller AR turbines at all distances from the tip, which may be caused by the higher upwind pass entrance velocities found in Section 4.2.2. The downwind pass portion of the torque profiles show varying behaviour between the different ARs, especially for the smallest AR case of a half, but this will be investigated later in Section 4.2.4.

The local power coefficient, which is effectively the average net torque, for each of the turbine slices was calculated and plotted versus the distance from the top of the turbine (Figure 24). This plot mirrors the results found in the torque profiles, with a reduction in the local power coefficient near the blade tips for all ARs. ARs two, four, and eight all recover from the tip power reduction at a similar rate and converge to a centre line performance for the remainder of the turbine height. ARs a half and one recover from the power reduction quicker than the higher AR turbines and continually increase

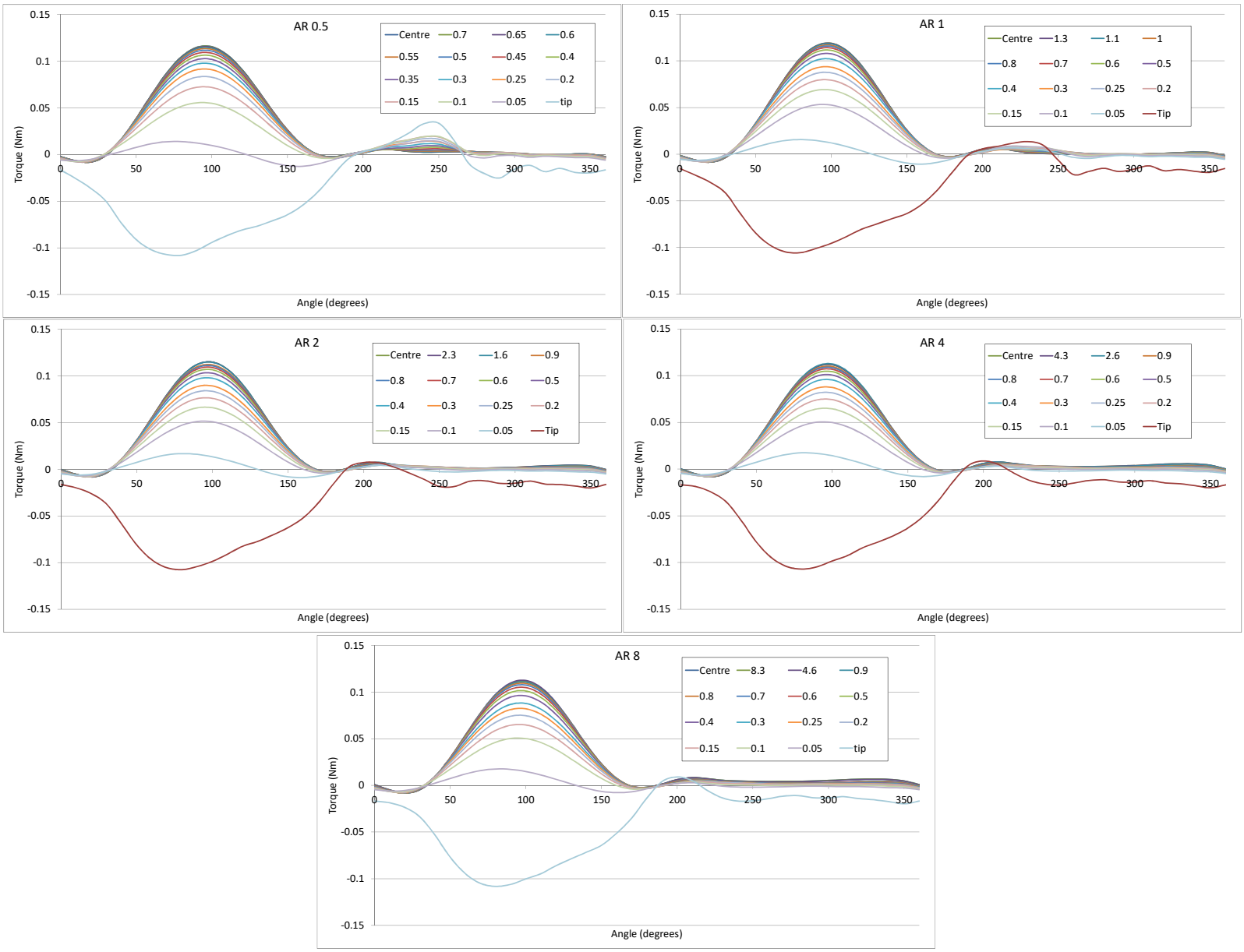

Figure 22: Torque slice profiles as a function of the blade position θ. The change in profile with distance (in meters) from the blade tip (Tip=0m) are displayed for each AR case.

in power output until reaching a maximum value at the turbine centre plane. This indicates that the distance away from the blade tips that is affected by the

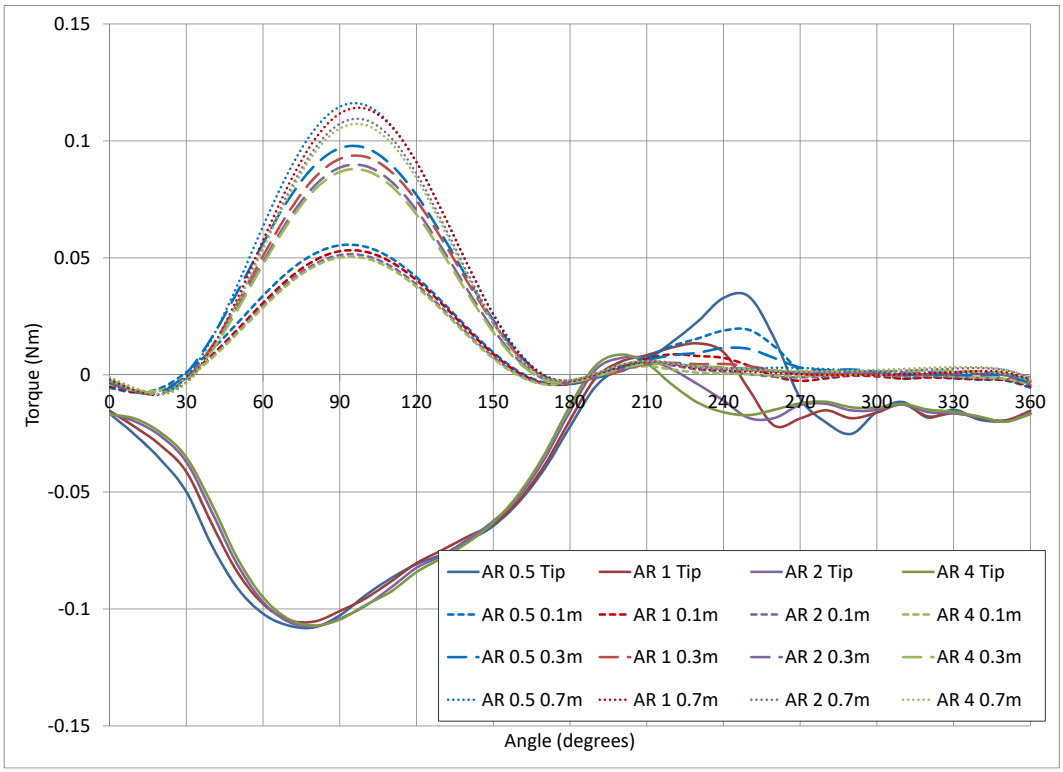

Figure 23: Torque slice profiles as a function of blade position θ, directly comparing a few slices between turbines of AR half, one, two, and four.

power reduction was constant for ARs greater than one at about one turbine radius away, while the full height of the smaller AR turbines are within reach of the tip effects.

The smallest AR case of a half, which has a height significantly shorter than the tip effect distance, showed a higher maximum power coefficient at approximately 0.37, 6% higher than the other AR cases. This increase in maximum power coefficient might be due to the significantly higher entrance velocity seen in the upstream divergence section of the results. Plotting these local power coefficients against a non-dimensionalized distance based on each

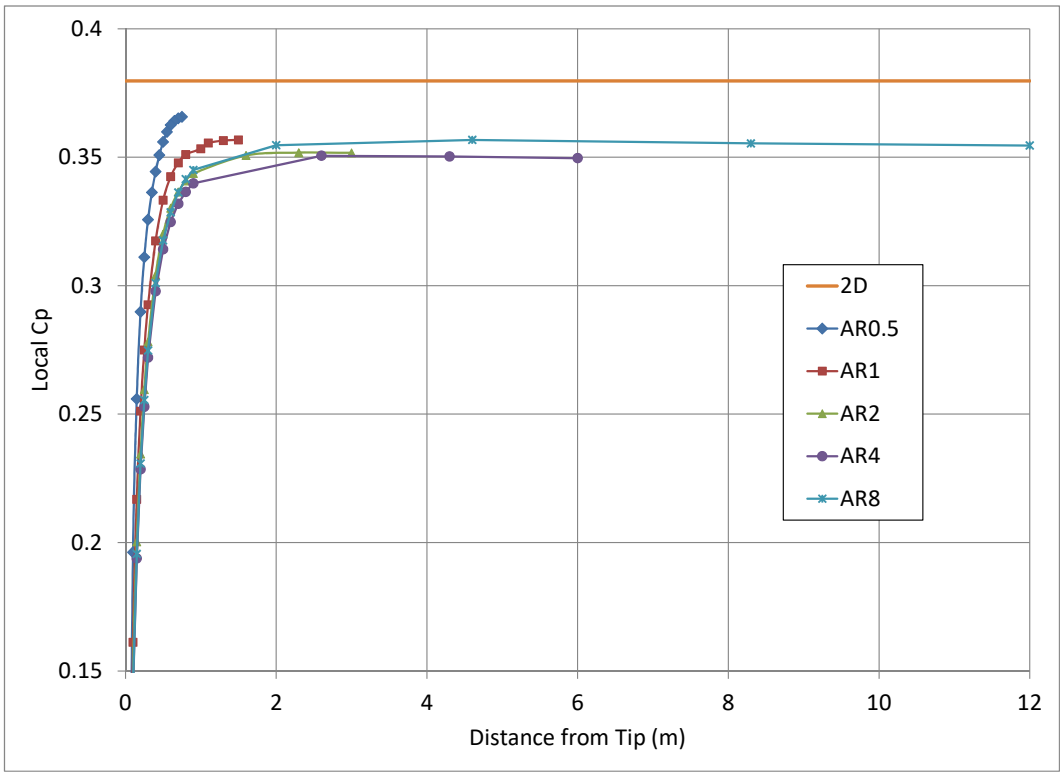

Figure 24: The change in local power coefficient as a function of distance from the blade tips in meters. All AR cases and the 2D power coefficient results are shown.

turbine ARs total height (Figure 25) shows that the total fraction of the turbine height affected by the tip power reduction was much greater for the smaller AR turbines. This would cause the smallest AR turbine of a half to have a lower overall power coefficient for the whole turbine as found in Section 4.1 even though the maximum output at the turbine centre line is higher.

From this analysis the overall turbine performance can be thought of as a combination of a tip impacted region with a reduced power output and a 2D region at the maximum power output for the remainder of the turbine height. A simple model can be created with a central 2D power coefficient set at 0.355

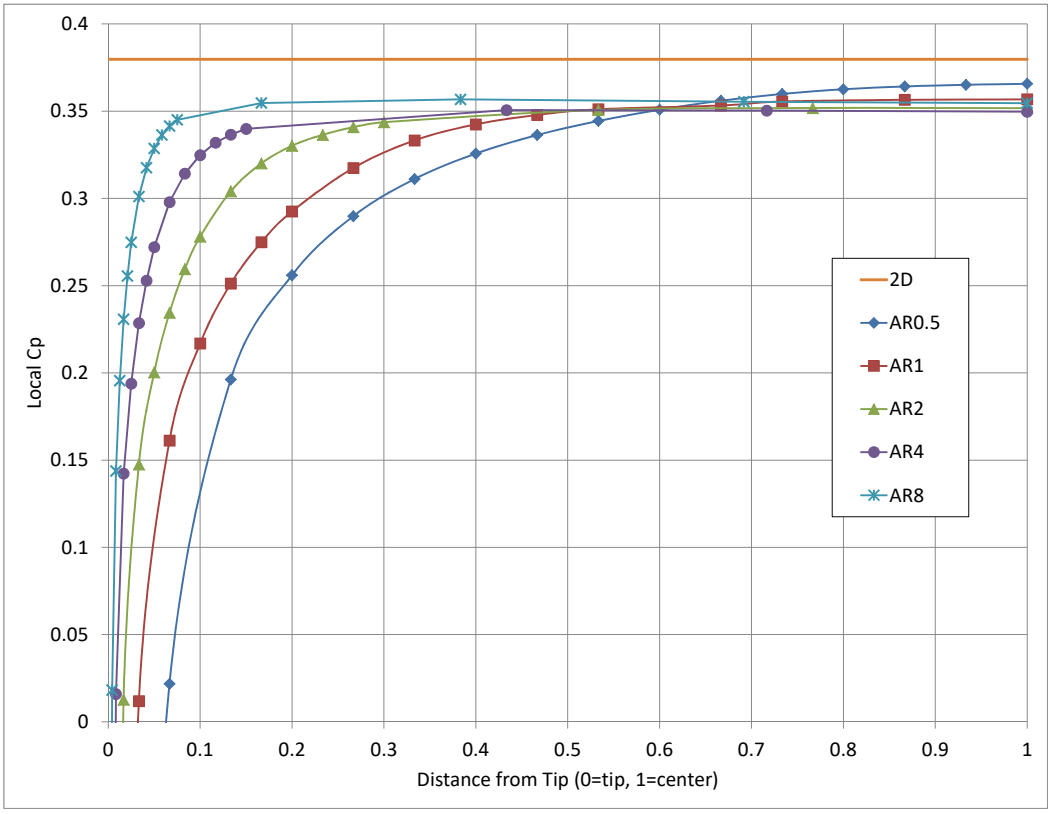

Figure 25: The change in local power coefficient as a function of distance from the blade tips. All AR cases and the 2D results are shown. The distance on the x axis is non-dimensionalized based on the total turbine height for each AR.

based on the average maximum power coefficients for turbine ARs of one and greater. The model can also have a tip region that impacts a fixed distance of the turbine height at 0.7m and has a set power coefficient of approximately 70% of the maximum at 0.25, based off integrating over the local power coefficient curve for ARs two, four and eight in the 0.7m tip region. Figure 26 compares the results from this simple model to the simulation results in this thesis, to see if it can potentially be used to predict the maximum peak power coefficient for a wider range of ARs. This simple model was able to roughly predict the peak power coefficients for the range of ARs used here, especially for turbines

with an AR greater than one. For ARs smaller than one that are completely affected by the tips and have no 2D region, this simple analysis is unable to account for the higher centre line performance and quicker tip recovery, causing it to underestimate the peak power coefficient.

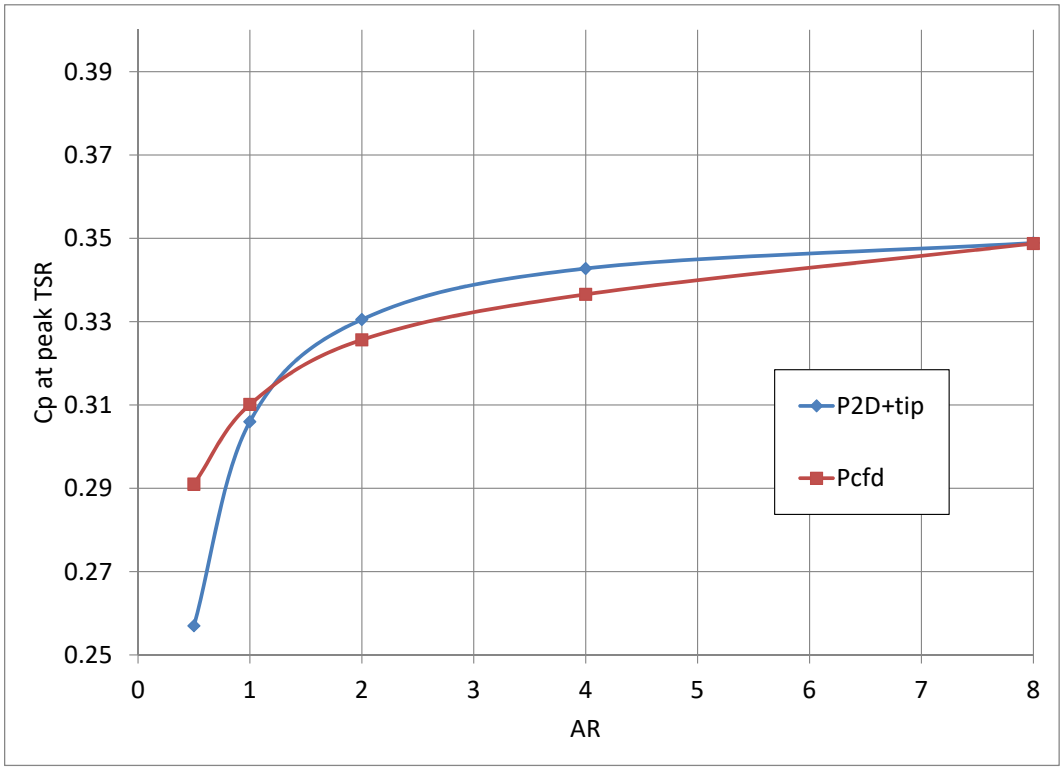

Figure 26: Plot comparing the simulation results to the simple model of a tip region contribution plus a 2D region contribution. The tip region contribution is based over a fixed distance from the top of the turbine and contributes power equivalent to 70% of the 2D power contribution.

Key findings of this analysis include that the reduced power of smaller AR turbines can be mainly attributed to the power reduction in the near tip region. This tip region affected a much greater fraction of the turbine height for the smaller AR turbines, which reduced the turbines overall power coefficient. As

a result, the higher AR turbines were more efficient at producing power, even though a smaller fraction of the upstream flow entered the upwind pass. This indicates that the additional flow divergence around higher AR turbines shown in Section 4.2.2 have a smaller impact on the power output of the turbine compared to the finite blade tip effects.

4.2.4 Turbine Internal Flow and Downwind Pass

In the torque curves for each of the turbine slices from Figure 22, the upwind pass was found to generate significantly more torque than the downwind pass. Calculating the net torque and converting it to a net power, the production difference between the upwind and downwind passes can be further analyzed (Figure 27). All AR cases have a similar power profile, except for the downwind pass portion of the AR half case, and there is an overall increase in power as the AR was increased. For all AR cases the upwind pass also produced the vast majority of the turbines power output. McLaren et al. (2012a) also found this large power differential and he attributed it to the velocity reduction that occurred inside the turbine between the two blade passes as well as the interaction of the shed vortices with the blades downstream.

The velocity reduction within the turbine can be examined from the CFD results for the various AR cases. The average velocity entering the upwind and downwind blade passes as well as the difference between them is shown in Figure 28. All AR cases saw a velocity drop occur within the turbine, with the AR one and two turbines matching for the lowest downwind pass entrance

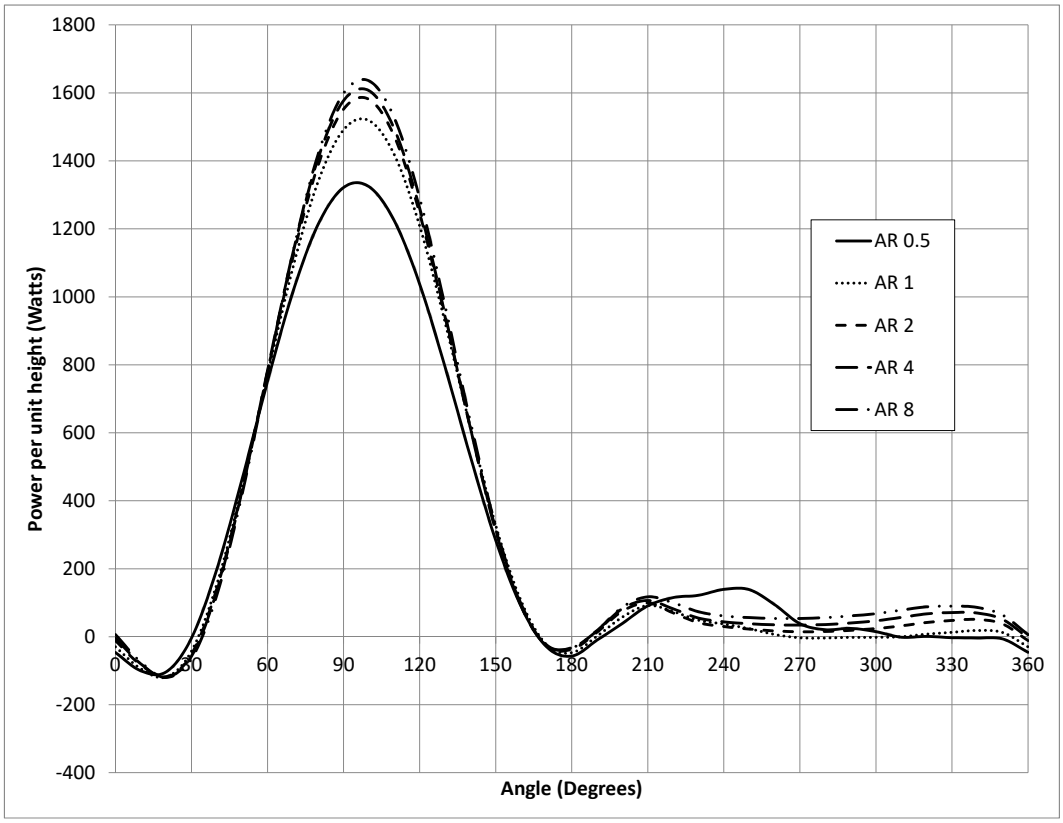

Figure 27: Net power profiles for different aspect ratios as a function of blade position. The power is shown per unit height to remove the impact of height change with AR.

velocity. The difference between the upwind and downwind pass entrance velocities showed the greatest velocity reduction occurred for a turbine of AR one, and the smallest for turbine AR of eight. Within the turbine all of the flow from the upwind pass can either go through the downwind pass or diverge around it by exiting through the top and bottom of the turbine. Therefore, the velocity reduction in Figure 28 between the upwind and downwind passes represents the amount of flow that escaped through the top of the turbine as only the top half of the turbine was simulated.

The volume flow rates through the top of the turbine (Table 2) show the

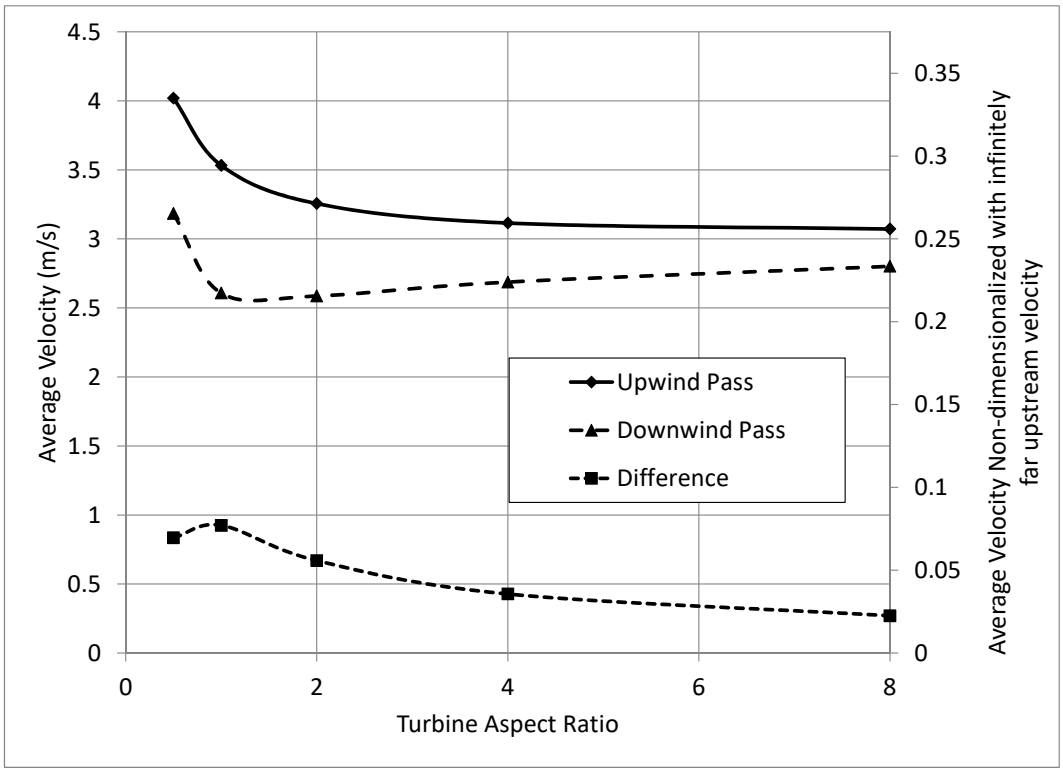

Figure 28: The change in average entrance velocity as a function of AR for the upwind and downwind passes. A difference curve is included to highlight the velocity reduction within the turbine centre.

Table 2: Table showing how the velocity change between the upwind and downwind passes related to the change in volume flow rate leaving the top of the turbine.

AR	ΔU inside turbine (m/s)	Volume flow rate through the turbine top (m^3/s)
0.5	0.835	3.32
1	0.925	6.37
2	0.670	8.53
4	0.428	9.84
8	0.270	10.5

effects of the upwind and downwind pass velocity differences. The volume flow rates increase monotonically as the AR increases, while the average velocity difference decreased for ARs of one and greater. The disconnect between the

velocity change and volume flow rates is due to the upwind and downwind passes changing area with AR, while the top area of the turbine stayed constant. As such, even though the velocity change was smaller between the two passes, the increased amount of total flow entering the turbine resulted in an increase in the flow rate exiting through the top of the turbine.

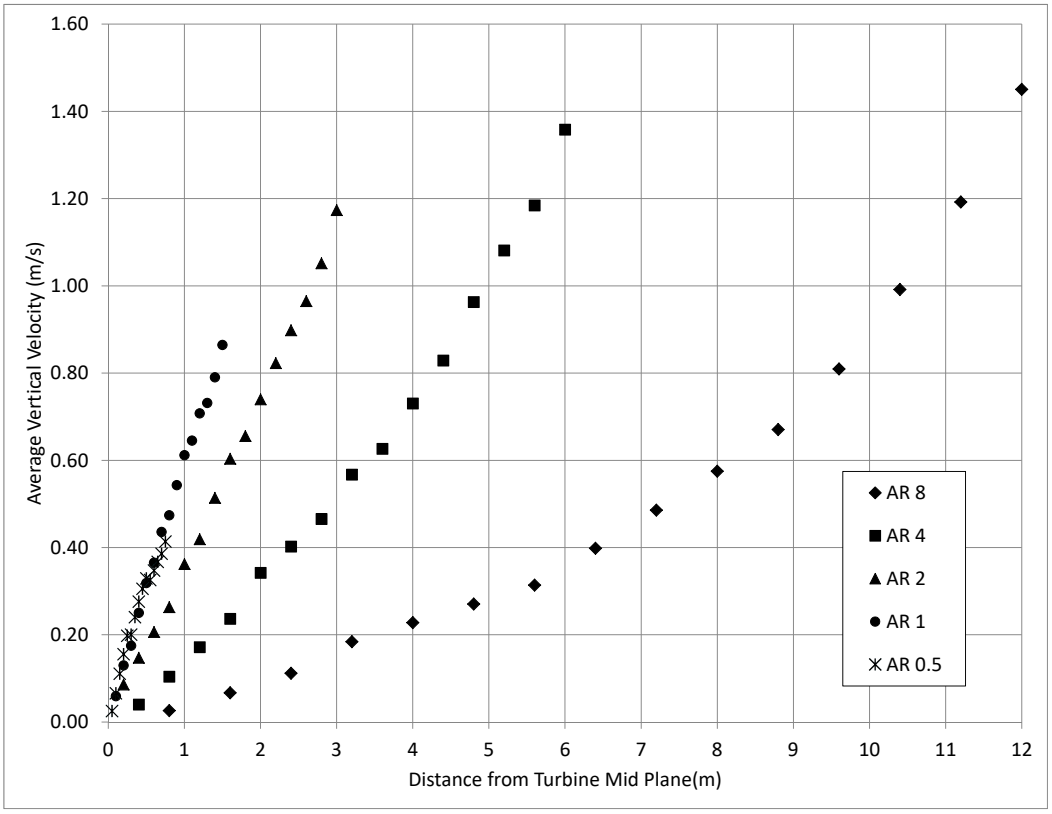

Figure 29: Accumulation of vertical velocity with distance from turbine centre for all ARs.

The vertical flow within the turbine increases from zero on the centre line to the values in Table 2 at the top of the turbine. Due to the resistance to flow entering the downwind pass, a fraction of the flow at each horizontal slice is diverted vertically, leading to this accumulation of vertical flow. Figure 29 shows this accumulation of average vertical velocity for the different AR cases.

For the small AR turbines of a half and one, the top flow roughly double showing this increase in accumulation of vertical flow. As the AR and the resulting height of the turbine is increased further, there appears to be a resistance to the accumulation of vertical flow develop, as the velocity no longer increases proportionally to the increase in area and has a slower accumulation rate near the turbine centre. The vertical flow is then controlled by the relative difference between the resistance to vertical accumulation, which changes with turbine height, and the resistance of the downwind pass, which is relatively fixed. This result can be clearly seen in the AR eight case in Figure 29 where the vertical velocity increases much slower near the turbine centre and transitions to match the accumulation rate of the smaller turbines near the blade tips. This results in the vertical velocity exiting the top of the turbine to still be larger, but the velocity difference between the upwind and downwind passes to be smaller for a higher AR turbine as shown in Figure 28. The extreme case of the 2D turbine can be thought of as having an infinite vertical flow resistance so it would accumulate zero vertical velocity and push all the flow through the downwind pass.

For the AR half case, the velocity difference between the upwind and downwind pass was lower than expected based on this simple resistance theory. To examine why this exception occurred, the vertical component of the velocity at the top plane of the turbine was analyzed for each AR case (Figure 30). For turbines of AR two and greater all the flow at the top plane is positive (upwards) and the magnitudes increase with AR corresponding with the values in Table 2. The AR one turbine has a small region of negative velocity in the

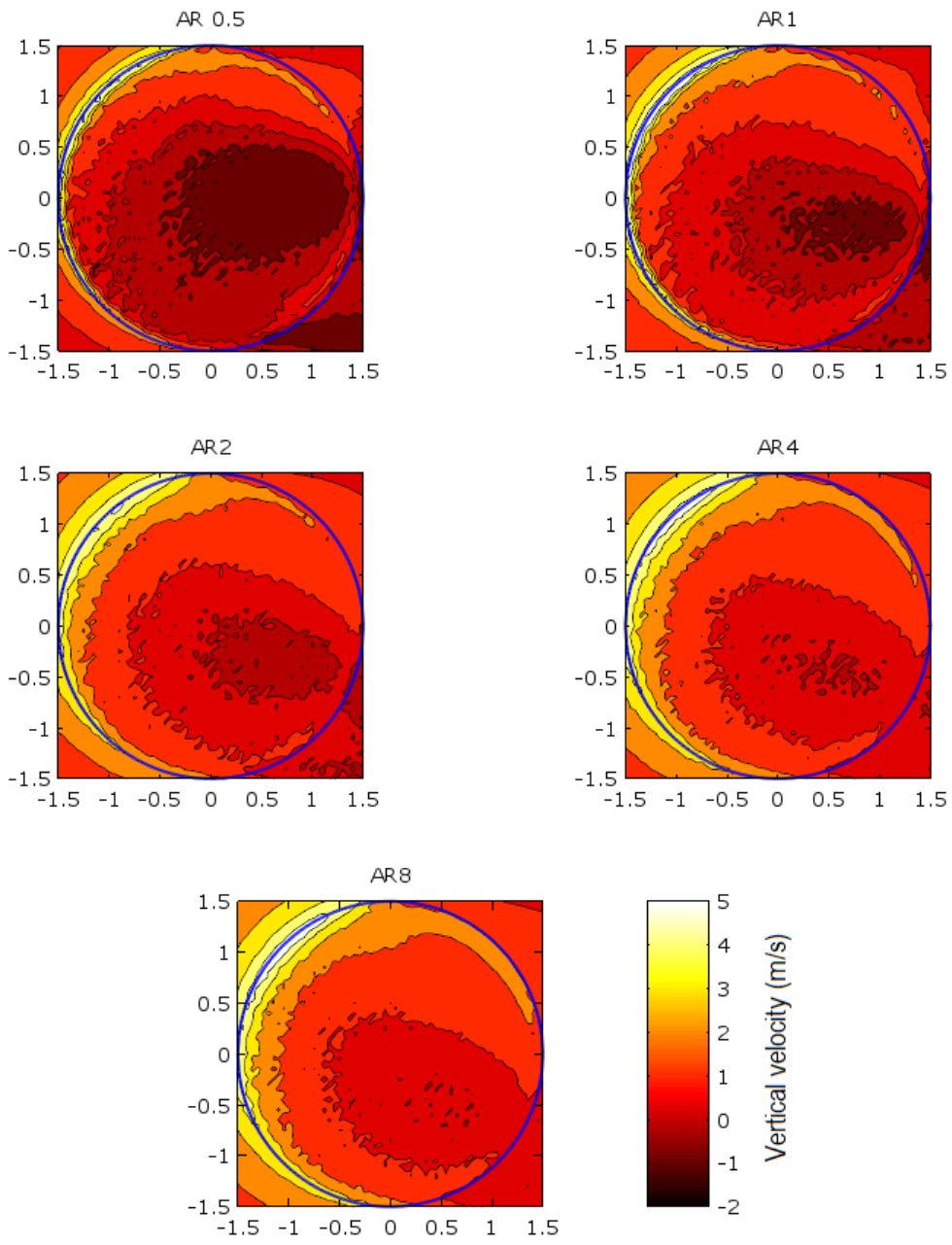

Figure 30: Contour plots of the vertical velocity at the top plane of the turbine for all ARs. The vertical velocities in m/s are based on the colour bar in the bottom right corner. The blue circle represents the turbine radius, the incoming flow is approaching the turbine from the left hand side of each plot, and the blades rotate around the turbine in a counter clock wise direction.

downwind portion of the turbine that is slightly offset toward the downstream oriented side of the turbine. The half AR turbine has a significantly larger region of negative velocity covering a large portion of the downwind half of the turbine. This area of negative vertical velocity represents flow re-entering the turbine after it diverged over the top of the upwind pass. The significant amount of flow re-entering the half AR turbine and traveling through the downwind pass caused the observed smaller than expected velocity difference between the upwind and downwind passes seen in Figure 28. This high speed flow re-entering the turbine for lower ARs also has the potential to increase the power output of the downwind pass.

The impact of these flow effects on the power output of the downwind pass were also analyzed (Figure 31). The power output of the downwind pass had similar profiles for turbine ARs greater than one, with a small proportional increase in overall output for each increase in AR. However, the lower AR turbines displayed a different power profile, with the most pronounced difference occurring for the AR half case. For the AR half case, there was a unique peak in power output between the blade angles of 210° and 270°, followed by a drop to zero torque at the tail end of the downwind pass. Results for the AR one case, are a combination of the AR half and higher AR profiles, as there was a small increase in power output between 210° and 270°, followed by the profile of the higher ARs near the end of the downwind pass.

In Figure 22, which showed torque profiles for turbine slices near the blade tips, the half AR case displays the same unique peak in downwind pass torque

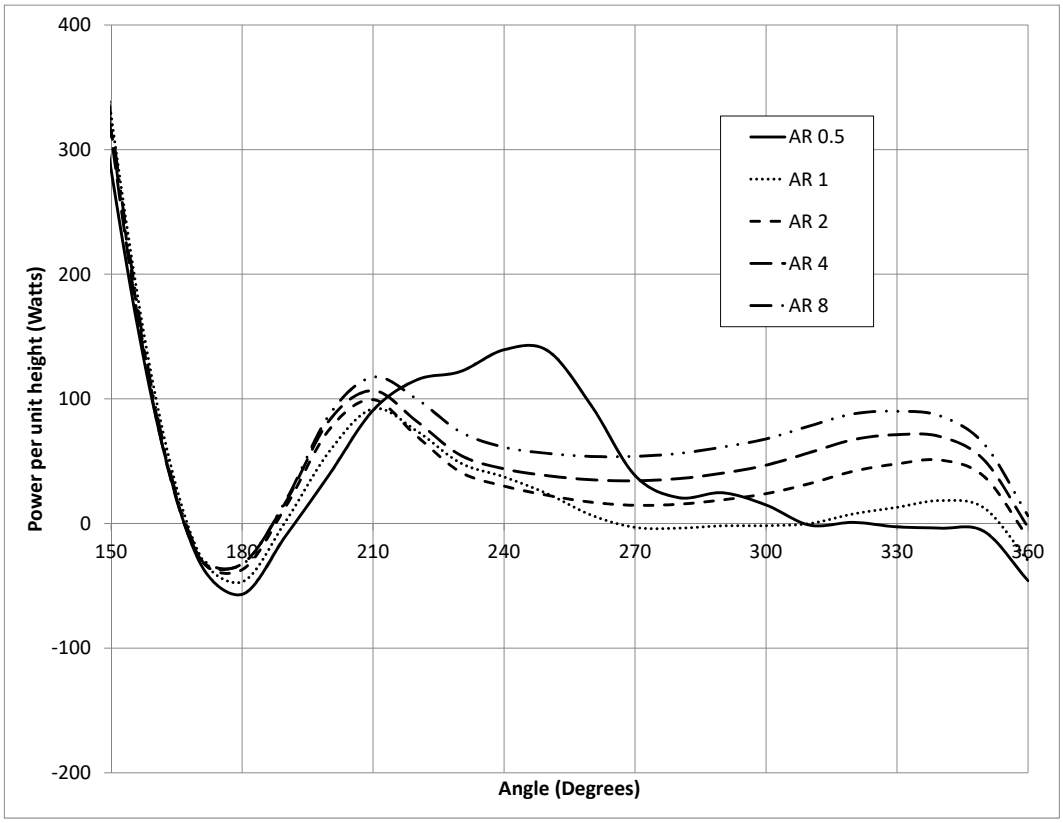

Figure 31: Torque as a function of blade position focusing on the downwind pass. All AR cases are shown.

output for the slices near the blade tips. The torque profiles for the turbine slices near the centre plane did not have the same unique peak in output, but instead matched with profile of the higher AR turbines. This indicates that the flow re-entering through the top of the AR half turbine, then travels through the tip region of the downwind pass causing the increased power production shown in Figure 31.

For all AR cases the power output of the downwind pass is significantly smaller than the upwind pass. For the AR eight case, the power output of the downwind pass is only 10% of the upwind power output. This drastic

change is partially due to the power being a function of the velocity cubed, so the 12% drop in velocity inside the turbine results in a loss of 30% maximum power potential for the downwind pass. In addition, as the velocity drops the TSR experienced by the blades along the downwind pass changes, causing the downwind pass to be operating at suboptimal performance. The biggest impact on the downwind pass performance is probably the blade interaction with the vortices shed upstream, which are not visible in the time averaged results in this study. The focus of this study was on the flow divergence so further investigation into the shed vortice interaction with the downwind pass blades was not performed. Therefore the results found in this study should predominately be used to better understand how the flow behaves within the turbine centre and the flow diverges around the downwind pass.

4.3 Results for Off Peak TSRs

The previous section focusing on how the flow divergence changed with AR, indicated that there may be some form of relationship between the flow divergence and power output of the turbine. By examining how the divergence and power changes with TSRs ranging from below peak power, at peak power and above peak power, the relationship between the two can be better understood. The majority of the results presented in this section are for a turbine of constant AR one at five different TSR values centred around the peak as shown in the AR one power curve in Figure 10.

4.3.1 Upstream Flow Divergence

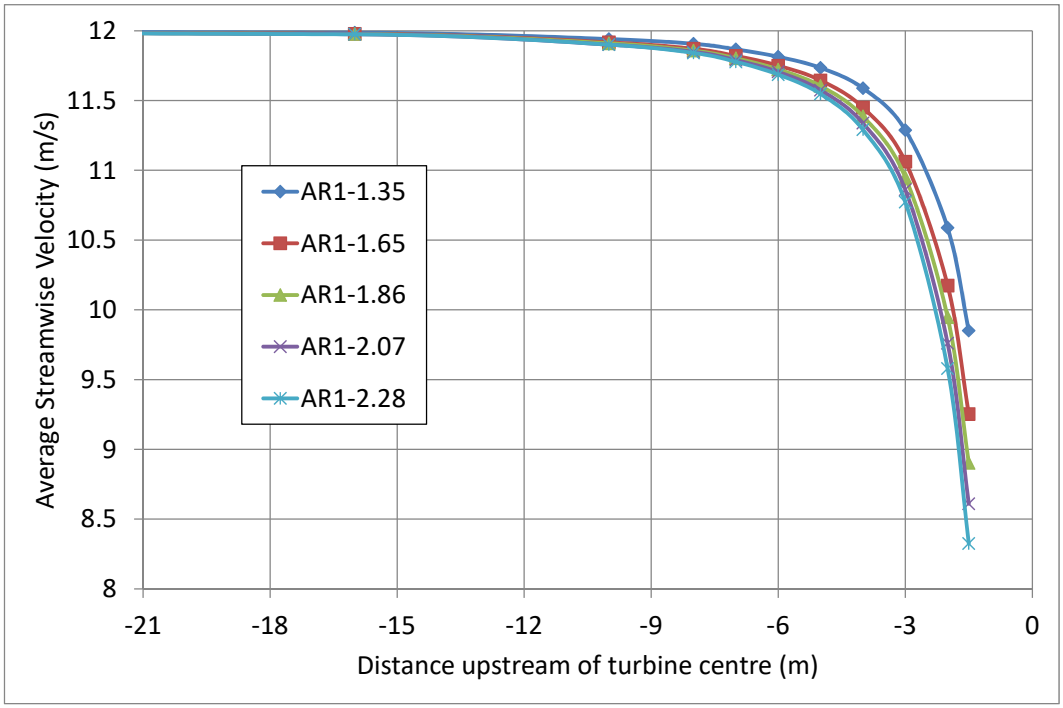

Figure 32: Plot showing the far field flow divergence for a turbine of AR one at five different TSR values.

The upstream flow analysis in Section 4.2.1 and 4.2.2 were repeated for a turbine of constant AR and changing TSRs. Figure 32 shows the trend for the divergence far upstream and less variation was seen compared to the impact of AR change. For all TSR cases there is almost no divergence three diameters upstream of the turbine. Between three diameters upstream and the upwind blade pass the divergence increases with higher TSRs.

The near field flow divergence was once again analyzed using planes to

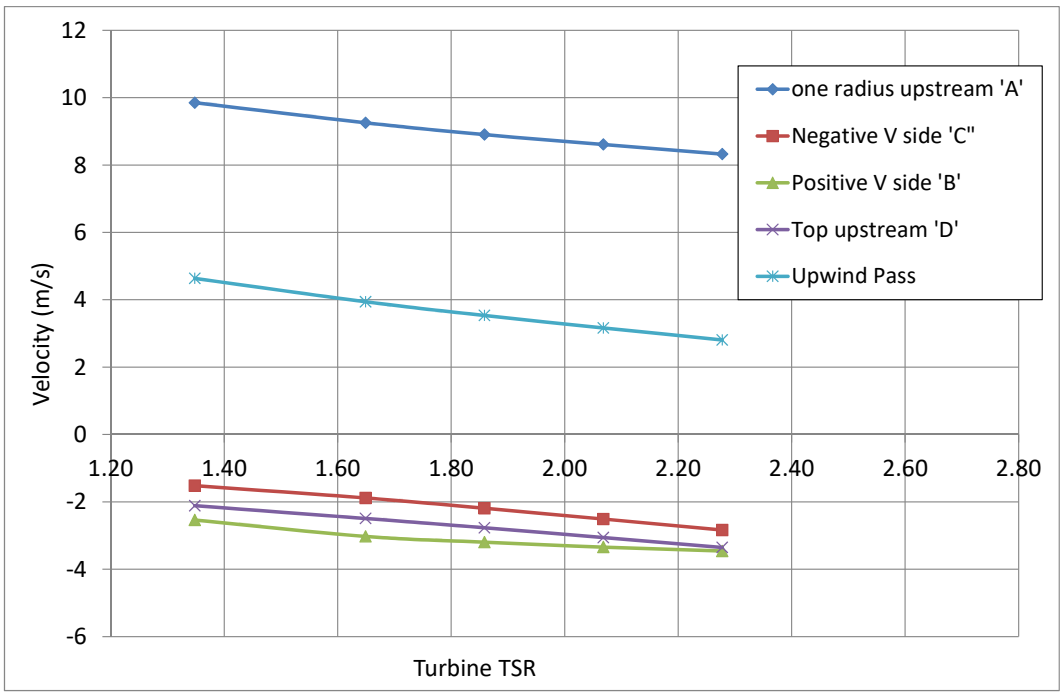

Figure 33: Plot showing the near field flow divergence for a turbine of AR one at five different TSR values. For a visual image of the different planes relative to a turbine refer to Figure 19.

create a virtual box around the upstream half of the turbine as shown in Figure 19. Figure 33 and Table 3 show the near field results and since the AR is held constant, the plotted velocities and tabulated flow rates directly mirror each other. Matching the results found farther upstream, the flow diverting through the sides and top planes increase with higher TSRs. The results indicate that a strong positive linear relationship exists between the upstream flow divergence and TSR.

Overall it is clear that as the TSR increases, more flow diverges around the

Table 3: Change of volume flow rates with TSR for different planes upstream of a turbine of AR one. All TSR volume flow rate results are based on a half area turbine due to the use of a symmetry plane in the model. For a visual image of the different planes relative to a turbine refer to Figure 19.

Label	Defined Planes	TSR				
		1.35	1.65	1.86	2.07	2.27
	Infinite Upstream (m^3/s)	54.0	54.0	54.0	54.0	54.0
A	One Radius Upstream (m^3/s)	44.3	41.6	40.1	38.8	37.5
B	Positive V side (m^3/s)	5.72	6.81	7.19	7.52	7.79
C	Negative V side (m^3/s)	3.42	4.24	4.93	5.65	6.38
D	Top upstream (m^3/s)	2.04	2.41	2.67	2.95	3.24
	Upwind pass (m^3/s)	32.75	27.85	24.97	22.37	19.84
	Percent of infinite upstream entering plane 1R upstream	82.0%	77.1%	74.1%	71.7%	69.3%
	Percent of infinite upstream entering the Upwind pass	60.6%	51.5%	46.2%	41.4%	36.7%
	Percent of 1R upstream exiting through Positive V side	12.9%	16.4%	18.0%	19.4%	20.8%
	Percent of 1R upstream exiting through Negative V side	7.72%	10.2%	12.3%	14.6%	17.0%
	Percent of 1R upstream exiting through Top Upstream	4.60%	5.78%	6.67%	7.62%	8.64%

turbine. This contradicts the idea that the divergence is directly impacted by the turbine power output, as shown in Table 4, for TSR values greater than 1.86 the power starts to decrease but the divergence does not. This indicates that a direct relationship between turbine power output and flow divergence does not exist, although there may still be a small indirect relationship between the two.

Table 4: Table highlighting how power coefficients change with TSR.

TSR	Cp	Cp relative to Peak Cp
1.35	0.228	0.74
1.65	0.298	0.96
1.86	0.310	1.00
1.35	0.284	0.92
1.35	0.247	0.80

4.3.2 Upstream Force

If the turbine power output is not a good method of estimating how much flow will diverge around it, instead the upstream force of the turbine on the air might be a better indicator. Based on the governing equations explained in Section 3.1, it is expected that the upstream flow divergence will be well correlated with the blade forces, specifically the forces in the upstream direction. The simplest values to acquire that would be a decent representation of this upstream force is the instantaneous upstream force generated by the blade at each position around the turbine. This would not account for the pressure field or full history of the flow, but should be enough to represent the majority of the upstream force while being much easier to analyze and acquire.

In addition, the force generated by the blades along the downwind pass can be assumed to be much smaller than those produced along the upwind pass based on radial force results found by McLaren (2011) that showed the downwind pass radial forces to be less than a quarter of the upwind pass.

Figure 34 shows the instantaneous upstream force generated by the blade with both blade position and turbine height along the upwind pass. The upstream force goes from zero at a blade position of 0° to maximum values at 90°, and back to zero at 180°. There is also a decrease in upstream force near the blade tips for all TSR cases that matches with the results seen for the torque in Section 4.2 Figure 22, and like the torque this tip force reduction is relatively constant for all AR cases. As the TSR changes for a constant AR turbine the upstream force profile keeps its overall shape, but sees an increase in magnitude for higher TSRs values. The TSR case of 1.35 has a slightly different profile with a distortion in the force profile at the start of the tip region between 90° and 150°. Hints of this distortion can be seen in McLaren (2011)'s experimental results where there is a slight kink in the average radial force at a TSR of 1.32 and blade position of 90°.

To analyze how the upstream force varies with both TSR and AR, the net upstream force over the upwind pass was integrated to a single value and non-dimensionalized via a coefficient of upstream force (Figure 35). For all AR turbines there was a roughly linear relationship between the upstream force coefficient and TSR. For Turbine ARs of one and greater the upstream force coefficient curves almost collapse onto each other with only a small increase in

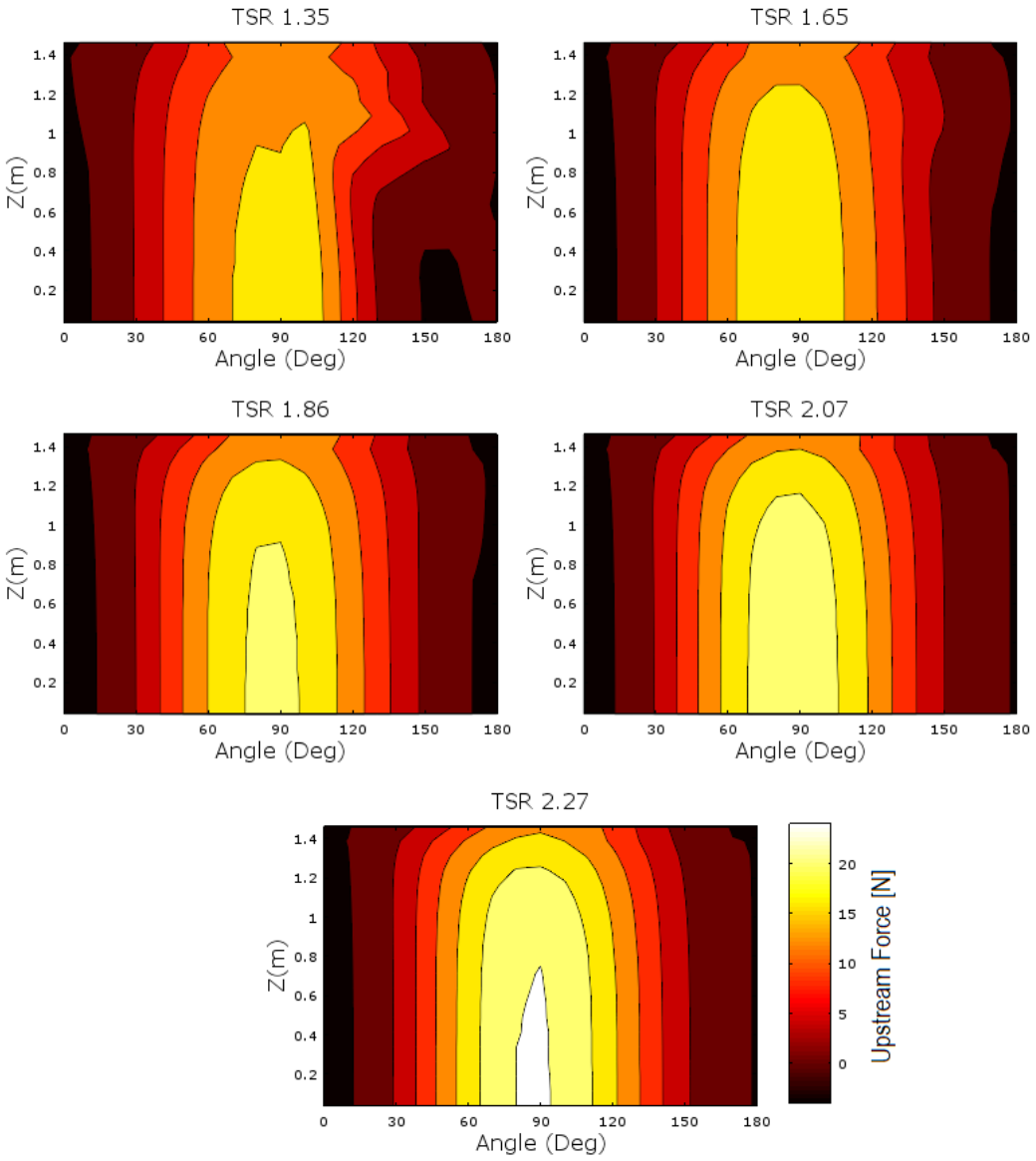

Figure 34: Contour plots showing the distribution of upstream force with turbine height and blade angle along the upwind pass. All plots are for the upper half of a AR one turbine each at a different TSR.

coefficients as the AR was increased. The half AR case has noticeably lower coefficients than the higher AR turbines, which is most likely due to the unique flow behaviour found for the smaller turbine in Section 4.2.

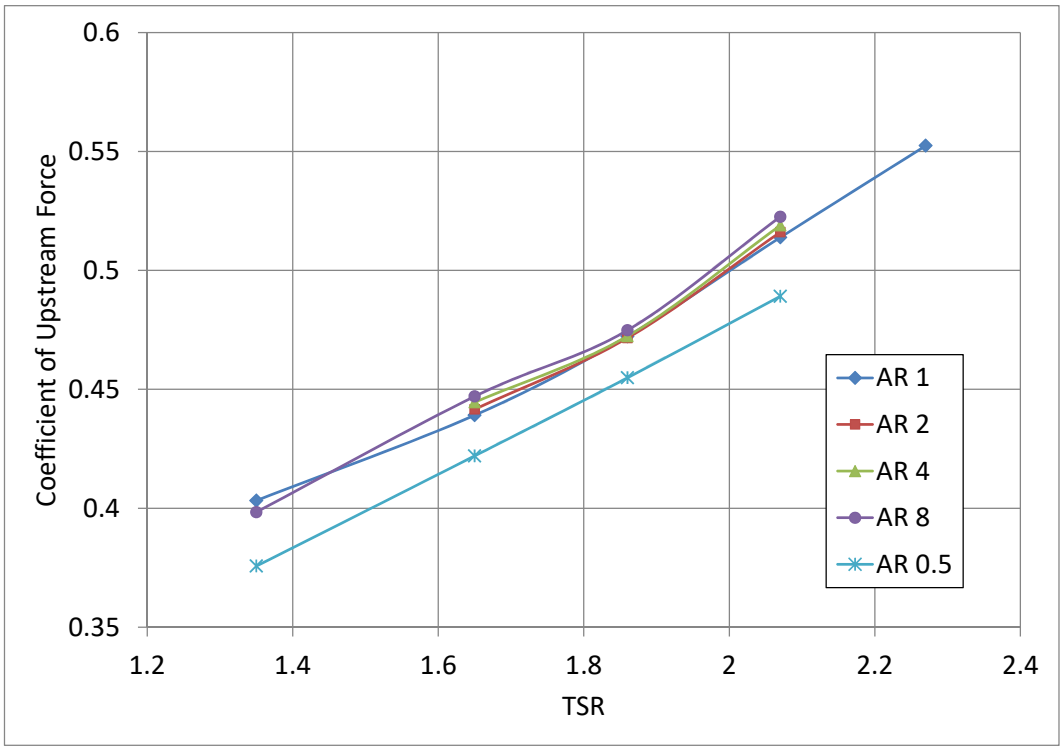

Figure 35: Plot of the upstream force coefficients verse the turbine TSR. The upstream force is plotted via the force coefficients to account for the area change between the different AR turbines.

The upstream force coefficients can also be plotted directly against the turbine divergence, represented inversely by the reduction in upwind pass entrance velocity (Figure 36). All AR cases have the entrance velocity decrease along with an increase in upstream force coefficient as the TSR was increased. The curves for ARs two, four and eight are almost the same with the AR half and one cases noticeably above them, similar to what was seen when the divergence was quantified in Section 4.2.2. These results do not reveal the exact relationship between the divergence and upstream force, but they strongly indicate that a direct relationship does exist between the two. A simple thought

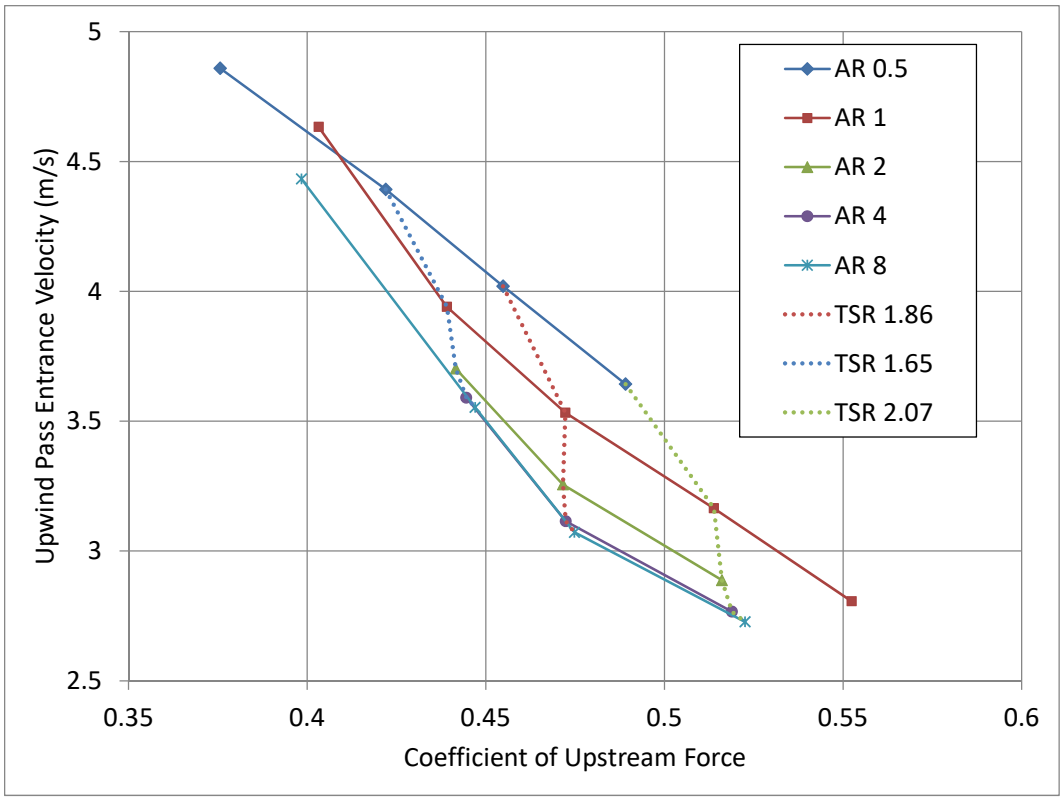

Figure 36: Plot of the upstream force coefficients verse the upwind pass entrance velocity inversely representing the flow divergence. The upstream force is plotted via the force coefficients to account for the area change between the different AR turbines. Solid lines are plotted such that they represent a constant AR with increasing TSR and dotted lines represent a constant TSR with increasing AR.

experiment can shed some light on how they could be related; starting with considering the divergence to be a function of how much of an obstacle the turbine is to the incoming flow. This turbine obstacle level is primarily a function of the total blade forces which are also responsible for determining the power output of the turbine, showing the indirect relationship between the divergence and power. The development of these blade forces are dependent on the local flow conditions seen by each small section of the blades, which in turn is ultimately a function of the overall flow divergence around the turbine.

Therefore the relationship between the upstream divergence and blade forces is likely an iterative function where they are dependent on each other and the full history of the flow and forces determine the values they converge to. This iterative relationship could be the reason that so many initial revolutions of the turbine need to be simulated before the flow conditions and blade forces converge to a steady solution.

Overall examining the upstream flow divergence at off peak TSRs showed that the turbine divergence was not a direct function of the turbine power output. As expected, the upstream divergence had a much stronger correlation with the blade force, specifically the upstream force of the blades on the air. Even a simplified value of the instantaneous upstream force for a number of blade positions along the upwind pass was shown to be an accurate indicator of the upstream flow divergence behaviour.

Chapter 5: Conclusions and Recommendations for Future Work

This research aimed to develop a better understanding of how the time averaged flow diverged in front of and through a VAWT. The use of 3D URANS simulations of high solidity VAWTs were examined to capture the full flow field around the turbine and provide an effective way to see how varying the turbine AR and TSR impacted this flow divergence.

5.1 Conclusions

The first major contribution of this research was a better understanding of how the flow diverged upstream of a VAWT. The vast majority of the upstream divergence occurred within two turbine diameters of the turbine centre and it diverged asymmetrically around the sides of the turbine. As the AR was increased more flow divergence occurred and it started to diverge further upstream. The divergence increase also showed an asymptotic behaviour with AR, where the results for an AR of four and eight were almost the same while ARs a half and one experienced the largest change. Examining the upstream divergence near the turbine in more detail showed that the turbine could be separated into two distinct sections; a highly 3D region near the blade tips where the velocities changed with height, and a 2D region away from the blade tips where there was minimal change in velocities with turbine height.

The distance which the tip region affected was constant for ARs greater than one and for lower ARs there was no 2D region as the full height of the turbine was impacted by the blade tips.

The turbine efficiency results were contradictory to the flow divergence results where a smaller AR turbine was shown to be less efficient at producing power, even though it had a noticeably higher fraction of the upstream flow entering the turbine. The second major contribution of this research was a better understanding of the power reduction experienced in the near tip region and why it was the reason for the contradiction between the flow divergence and turbine efficiency. The effective distance of the tip power reduction was constant for ARs greater than one, similar to the 3D tip region found for the divergence. This resulted in a smaller AR turbine having a greater fraction of the total height affected by the tip power reduction, resulting an overall lower efficiency. There was a higher centre line performance found for the smaller AR turbine due to the higher entrance velocity, but the impact of the tip effects were more dominate in determining the overall turbine efficiency.

The results found from the upstream flow divergence and tip region analysis also highlighted whether McLaren's correction factors represented the actual physics of the flow. The lower upstream divergence seen for a low AR turbine was contradictory to the theory behind the κ correction factor, showing it to not be an accurate physical representation of the flow. The power reduction at the blade tips that effectively reduced the height of the turbine producing max power matched well with the theory behind the τ correction factor. However,

the τ correction factor was based on a percentage of the turbine height rather than a fixed distance from the tips as found here.

The next major contribution was a greater understanding of the flow behaviour within the centre of the turbine. There was an accumulation of vertical flow that was dependent on the relative difference between the downwind pass resistance and the resistance to vertical flow. As the AR (turbine height) was increased, a higher resistance to vertical flow accumulations was found resulting in a smaller velocity reduction between the upwind and downwind passes. For the lowest AR, unique flow behaviour was shown to occur, where high speed flow that had diverged over the top of the upwind pass re-entered through the top of the turbine and traveled through the tip region of the downwind pass.

Overall the power output was still much lower for the downwind pass due in part to this velocity reduction. Since the power is a function of the velocity cubed, a small velocity drop resulted in a significant impact on the maximum power potential and also changed the TSR for the downwind pass, such that it operated at suboptimal conditions. The interactions of the vortices shed upstream with the downstream blades was also expected to have a large impact on the power output of the downwind pass, but as the focus of this study was researching the overall flow divergence it was not investigated.

The last major contribution was a greater understanding of the driving factors behind the flow divergence around a VAWT. From earlier results, there appeared to be a relationship between the divergence and turbine power out-

put, but from analysis of the divergence change with TSR this relationship was found to not be direct. The blade forces, specifically the force generated in the upstream direction, appeared to have a strong linear relationship with the flow divergence behaviour. These blade forces were also responsible for the power output of the turbine, so the indirect relationship between the power and divergence does exist.

5.2 Recommendations for Future Work

The first recommendation for future work would be to use the same dataset as used in this study to further explore the flow behaviour around a VAWT, specifically the details of the unsteady flow. This would strengthen the understanding of how the dynamic AoA changes with blade position, and the shedding of vortices downstream impact the power output of the turbine. More specifically, the vortex development around the end of the blade and their shedding downstream could help improve the understanding of how the unsteady aspect of the flow impacts the flow divergence and power reduction experienced by the blade tips.

The other suggested future work would be to investigate ways to lessen the power reduction experienced by the blade tips. This could be done by either altering the blade tip geometry parameters such as tip platform shape, blade thickness, or chord length, or using wingtip devices such as winglets or end-plates. Due to the highly dynamic nature of the AoA experienced by the

blades, adding winglets or end-plates is not expected to make a large impact on the tip power reduction. An effective way to investigate these different tip shapes would be through the use of 3D CFD analysis very similar to that performed in this study. If the impact of the tip power reduction could be reduced for a small AR turbine while keeping the benefit of a higher entrance velocity as found in this study, then the performance of small scale VAWTs could be improved.

References

Akins, R. E. (1989). *Measurements of surface pressures on an operating vertical-axis wind turbine* (Tech. Rep. No. SAND89-7051). Lexington, Virginia: Sandia National Laboratories.

Alaimo, A., Esposito, A., Messineo, A., Orlando, C., & Tumino, D. (2015). 3d cfd analysis of a vertical axis wind turbine. *Energies*, *8*, 3013–3033. doi: 10.3390/en8043013

Balduzzi, F., Drofelnik, J., Bianchini, A., G., F., L., F., & S., C. M. (2017). Darrieus wind turbine blade unsteady aerodynamics: a three-dimensional navier-stokes cfd assessment. *Energy*, *128*, 550–563.

barth, T. J., & Jesperson, D. C. (1989). The design and application of upwind schemes on unstructured meshes. In *27th aerospace science meeting.* (AIAA(89-0366))

Battisti, L., Zanne, L., Dell'Anna, S., Dossena, V., Persico, G., & Paradiso, B. (2011). Aerodynamic measurements on a vertical axis wind turbine in a large scale wind tunnel. *Journal of Energy Resources Technology*, *133*.

Bhargav, M. M., Kishore, V. R., & Laxman, V. (2016). Influence of fluctuating wind conditions on vertical axis wind turbine using a three dimensional cfd model. *Journal of Wind Engineering and Industrial Aerodynamics*, *158*, 98–108.

Blades, E. L., & Marcum, D. L. (2006). A sliding interface method for unsteady unstructured flow simulations. *International Journal for Numerical Methods in Fluids*, *53*, 507-529.

Bravo, R., Tullis, S., & Ziada, S. (2007). Performance testing of a small vertical-axis wind turbine. In *Proceedings of the 21st canadian congress of applied mechanics* (pp. 470–471).

Brochier, G., Fraunie, P., Beguier, C., & Paraschivoiu, I. (1986). Water channel experiments of dynamic stall on darrieus wind turbine blades. *AIAA Journal of Propulsion and Power*, *2*, 445-449.

Chowdhury, A. M., Akimoto, H., & Hara, Y. (2016). Comparative cfd analysis of vertical axis wind turbine in upright and tilted configuration. *Renewable Energy*, *85*, 327–337.

Fiedler, A. (2009). *The effects of blade pitch and mount point offset on vertical axis wind turbine performance* (Unpublished master's thesis). McMaster University, Hamilton, Ontario, Canada.

Fiedler, A., & Tullis, S. (2009). Blade offset and pitch effects on a high solidity vertical axis wind turbine. *Wind Engineering*, *33*(3), 237–246.

Fujisawa, N., & Shibuya, S. (2001). Observations of dynamic stall on darrieus wind turbine blades. *Journal of Wind Engineering and Industrial Aerodynamics*, *89*, 201–214.

Ghasemian, M., & Nejat, A. (2015). Aero-acoustics prediction of a vertical axis wind turbine using large eddy simulation and acoustic analogy. *Energy*, *88*, 711–717.

Hofemann, C., Ferreira, C. S., Dixon, K., Bussel, G., Kuik, G., & Scarano, F. (2008). 3d stereo PIV study of tip vortex evolution on a VAWT. In *Proceedings of the european wind energy conference and exhibition.*

Howell, R., Qin, N., Edwards, J., & Durrani, N. (2010). Wind tunnel and numerical study of a small vertical axis wind turbine. *Renewable Energy*, *35*, 412–422.

Jones, W. P., & Launder, B. E. (1972). The prediction of laminarization with a two-equation model of turbulence. *International Journal of Heat and Mass Transfer*, *15*, 301–314.

Lam, H. F., & Peng, H. Y. (2016). Study of wake characteristics of a vetical axis wind turbine by two and three-dimensional computational fluid dynamics simulations. *Renewable Energy*, *90*, 386–398.

Lee, Y. T., & Lim, H. C. (2015). Numerical study of the aerodynamic performance of a 500 w darrieus-type vertical-axis wind turbine. *Renewable Energy*, *83*, 407–415.

Li, Q., Maeda, T., Kamada, Y., Murata, J., Furukawa, K., & Yamamoto, M. (2016). The influence of flow field and aerodynamics forces on a straight-bladed vertical axis wind turbine. *Energy*, *111*, 260–271.

Li, Q., Maeda, T., Kamada, Y., Shimizu, K., Ogasawara, T., Nakai, A., & T., K. (2017). Effect of rotor aspect ratio and solidity on a straight-bladed vertical axis wind turbine in three-dimensional analysis by panel method. *Energy*, *121*, 1–9.

Mathur, S. R. (1994). Unsteady flow simulations using unstructured sliding meshes. In *Aiaa fluid dynamics conference.*

McLaren, K. (2011). *A numerical and experimental study of unsteady loading of high solidity vertical axis wind turbines* (Unpublished doctoral dissertation). McMaster University, Hamilton, Ontario, Canada.

McLaren, K., Tullis, S., & Ziada, S. (2012a). Computational fluid dynamics simulation of the aerodynamics of a high solidity small-scale vertical axis wind turbine. *Wind Energy*, *15*, 349–361.

McLaren, K., Tullis, S., & Ziada, S. (2012b). Measurement of high solidity vertical axis wind turbine aerodynamic loads under high vibration response conditions. *Journal of Fluids and Structures*, *32*, 12–26.

Menter, F. R. (1994). 2-equation eddy-viscosity turbulence models for engineering applications. *AiAA Journal*, *32*(8), 1598–1605.

Nini, M., Motta, V., Bindolino, G., & Guardone, A. (2014). Three-dimensional simulation of a complete vertical axis wind turbine using overlapping grids. *Journal of Computation and Applied Mathematics*, 1598–1605.

Orlandi, A., Collu, M., Zanforlin, S., & Shires, A. (2015). 3d urans analysis of a vertical axis wind turbine in skewed flows. *Journal of Wind Engineering and Industrial Aerodynamics*, *147*, 77–84.

Paraschivoiu, I. (1981). *Double-multiple streamtube model for darrieus in turbines* (Tech. Rep.). varennes, Quebec: Institut de Recherche d'Hydro-Quebec.

Paraschivoiu, I. (2002). *Wind turbine design: with emphasis on darrieus concept*. Polytechnic International Press.

Raw, M. J. (1996). Robustness of coupled algebraic multigrid for the navier-stokes equations. In *34th aerospace science meeting.* (AIAA(96-0297))

Strickland, J. H. (1975). *The darrieus turbine: A performance prediction model using multiple streamtubes* (Tech. Rep. No. SAND75-0431). Albuquerque, New Mexico: Sandia National Laboratories.

Subramanian, A., Yogesh, S. A., Sivanandan, H., Giri, A., Vasudevan, M., Mugundhan, V., & K., V. R. (2017). Effect of airfoil and solidity on performance of small scale vertixal axis wind turbine using three dimensional cfd model. *Energy*, *133*, 179–190.

van Kuik, G. (2007). The lanchester-betz joukowsky limit. *Wind Energy*, *10*, 289–291.

Wilcox, D. C. (1993). *Turbulence modeling for cfd*. DCW Industires Inc.

Appendix A: Inviscid Potential Flow Results

In the results section 4.2.1, the upstream flow divergence around the 2D turbine was compared to the inviscid solution for the flow around a cylinder. In the velocity component formulas for the inviscid flow around a rotating cylinder shown below, the circulation (Γ) value found in the angular velocity formula represents the magnitude of the cylinders rotation. When deciding what circulation value to use for the comparison, different values were tested to see how they impact the upstream divergence (Figure 37). As the circulation value is increased, more flow diverts from one side of the turbine to the other. When the average is taken over this line though, all the different circulation values have the exact same average velocity as shown in Table 5. Therefore the upstream divergence was found to be independent of the circulation value for the inviscid solution for flow around a 2D cylinder. As such when doing the comparison to the 2D simulation results in section 4.2.1, there was no clarification on an exact circulation value for the comparison.

$$V_r = U_\infty(1 - \frac{R^2}{r^2})cos(\theta)$$

$$V_\theta = U_\infty(1 + \frac{R^2}{r^2})sin(\theta) + \frac{\Gamma}{2\pi r}$$

$$V_x = V_r cos(\theta) + V_\theta sin(\theta)$$

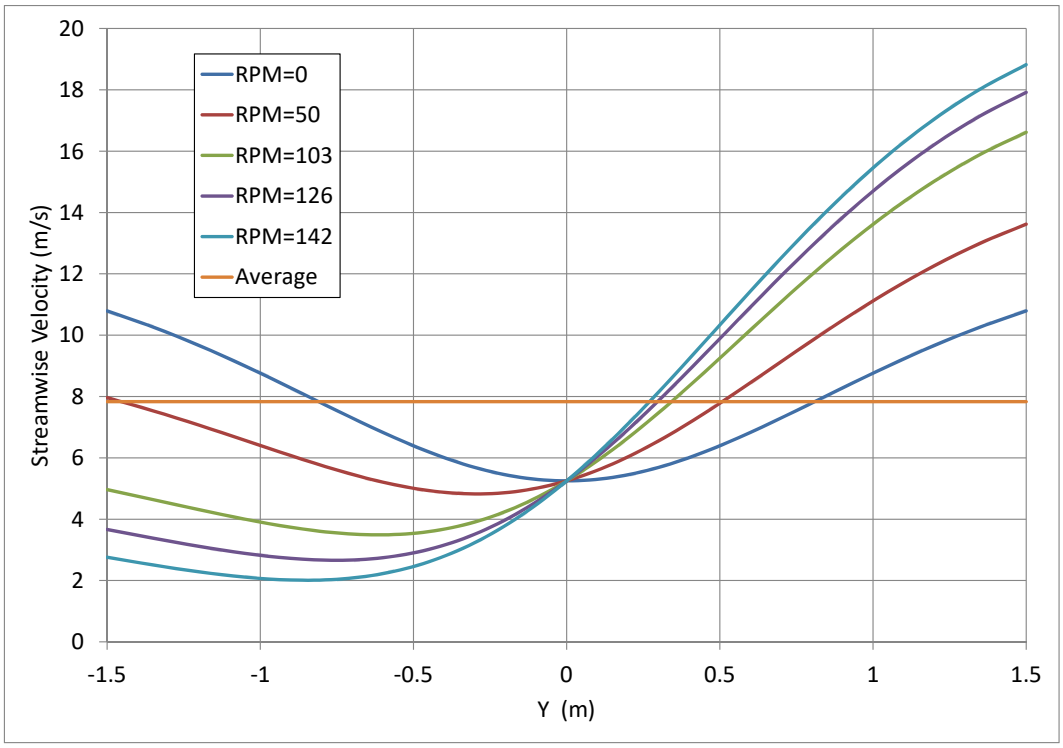

Figure 37: Plot showing the streamwise velocity for a line two meters upstream of a 2D rotating cylinder. The velocity profile along the line for different circulation (cylinder rotation) magnitudes are shown for comparison.

Table 5: Table showing the upstream flow divergence results for the inviscid flow around a 2D rotating cylinder at different circulation values. The calculations are for a line equal to the cylinders 2D projected area, two meters upstream of the cylinder.

RPM	Circulation	Average Velocity Over Plane 2m Upstream
0	0.00	7.83
50	74.02	7.83
103	152.49	7.83
126	186.54	7.83
142	210.22	7.83